ANNALS OF GEOPHYSICS, 68, 5, DM582, 2025; doi:10.4401/ag-9282
OPEN ACCESS

SEA-SEIS ocean bottom seismometer network in the Northeast Atlantic: Performance, data properties, biological observations and audification innovations

Janneke I. de Laat[*,1], Sergei Lebedev[2,3], Raffaele Bonadio[2,3], Thomas A.J. Merry[2], Maria Tsekhmistrenko[4], David Stalling[5], the SEA-SEIS Team[**,3]

(1) j.i.delaat@utwente.nl, Department of Applied Earth Sciences, ITC, University of Twente, Enschede, The Netherlands
(2) Department of Earth Sciences, University of Cambridge, Cambridge, United Kingdom
(3) Dublin Institute for Advanced Studies, Dublin, Ireland
(4) Department of Earth Sciences, University College London, London, United Kingdom
(5) Independent Researcher, Mullingar, Ireland

** For further information regarding the team, please visit https://sea-seis.ie.

Article history: received January 31, 2025; accepted September 12, 2025

Abstract

Project SEA-SEIS deployed 18 ocean-bottom seismometers (OBS) in the Northeast Atlantic Ocean, bounded by Ireland and Britain to the east and Iceland and the Mid-Atlantic Ridge to the northwest. The 3-component, broadband instruments, each with an additional broadband hydrophone, were deployed for 19 months, from September-October, 2018, to April-May, 2020. A key goal of the deployment was to advance our understanding of the structure and dynamics of the North Atlantic lithosphere and underlying mantle, origins of the North Atlantic Igneous Province and the morphology of the Iceland Plume. Fourteen of the 18 instruments were retrieved, with 2 of the 14 showing problems with the data that limited their use. The remaining 12 OBSs provided continuous, 19-month recordings. As observed elsewhere, the OBS noise level is higher than at land stations, due to the poorer coupling to the seafloor and noise from ocean currents and waves. Data pre-processing comprised the clock-drift correction, horizontal-component-orientation determination and compliance- and tilt-noise suppression. Every seismometer came up with multiple sea-creature species attached to it, bringing useful information on their habitats. At depths up to ~1200 m, octopuses used the OBSs to lay and guard their eggs. In addition to conventional processing, seismic data was also transformed to audible frequency ranges. New methods for translating the data's spatial information to ambisonic surround sound were developed. The audifications offered a new perspective on the data and underpinned a productive art-science collaboration and an outreach program.

Keywords: Seismology; Seismometer; OBS; North Atlantic; Performance report

1. Introduction

The majority of the world's seismic stations are located on land, and the global data coverage shows major gaps in the oceans. To address this imbalance, Ocean Bottom Seismometers (OBSs) have been developed and deployed in a growing number of locations (e.g., Suyehiro et al., 1992; Beaudin and Montagner, 1996; Collins et al., 2001; Laske et al., 2009; Yang et al., 2012; Stähler et al., 2016; Geissler et al., 2017; Agius et al., 2018; Barcheck et al., 2020; Jeddi et al., 2021; Parisi et al., 2024; Tsekhmistrenko et al., submitted), enabling the collection of seismic data directly from the seafloor and offering new insights into the structure and dynamics of the oceanic crust and mantle (e.g., Agius et al., 2018; Bonadio et al., 2018; Janiszewski et al., 2019; Harmon et al., 2020; Tsekhmistrenko et al., 2021). In the Northeast Atlantic, some relatively small broadband OBS deployments have taken place, such as a 3-month experiment south of Iceland (Dahm et al., 2006) and experiments between mainland Norway and Svalbard (Czuba et al., 2011, Barreyre et al., 2023) and northwest of Ireland (Craig et al., 2019). However, no large-scale broadband seismic data have been collected, until now, from the Northeast Atlantic Ocean (Fig. 1).

The project SEA-SEIS (Structure, Evolution And Seismicity of the Irish offshore) was designed to fill the data gap in this important region and deployed 18 OBSs between Ireland and Britain to the east and Iceland and the Mid-Atlantic Ridge to the north and west (Fig. 1). The main aim of the deployment, led by the Dublin Institute for Advanced Studies, was to advance our understanding of the deep structure and dynamic processes that have shaped the North Atlantic region, including the Iceland Hotspot.

The SEA-SEIS deployment has produced unique broadband seismic data that offers new insights into the structure, evolution and seismicity of the region. The new data also contains numerous vocalizations of fin and blue whales. The experiment also produced ad hoc marine biology observations via the numerous sea creatures that attached to the OBSs during the deployment and came onboard with the instruments.

The first goal of this paper is to describe the design and instrumentation of the experiment, the network's performance, and the main problems encountered. We then report on the main parts of the data pre-processing completed. Finally, we summarize the sea-creature observations and our original work on the audification of seismic signals, which was completed in collaboration between seismologists and a sound artist and engineer.

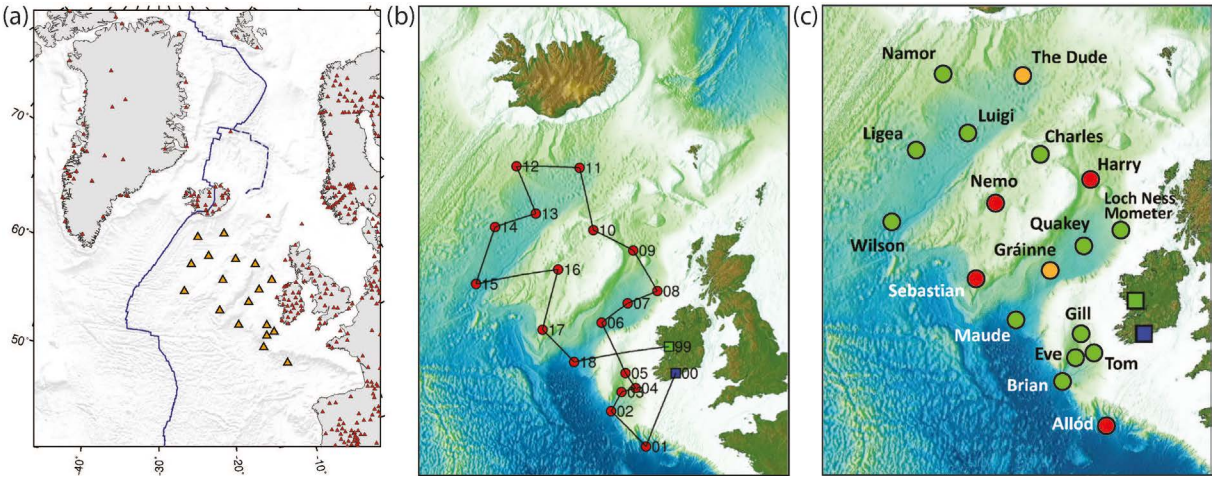

Figure 1. (a) Map of the Northeast Atlantic region, showing the (open access) land stations in the region (small red triangles), and the location of the 18 OBSs deployed by the project SEA-SEIS (large orange triangles). (b) The locations of the SEA-SEIS stations (red circles) and the route of the deployment cruise. The blue square indicates the departure point (Cobh, near Cork), the green square – the arrival point (Galway). (c) The SEA-SEIS stations are labelled by their names, as given to them by school children in Ireland and Italy (Lebedev et al., 2019). FDSN-standard station codes are listed in Table 1. Green: successfully retrieved OBSs, red: OBSs that failed to come up, orange: OBSs that were retrieved but showed problems with the data (Section 4.2.1).

2. The SEA-SEIS network

The 18 OBS were deployed from RV Celtic Explorer, operated by the Marine Institute (https://www.marine.ie), between 17 September and 5 October 2018. The recovery cruise – also on RV Celtic Explorer – took place between 25 April and 13 May 2020. Fourteen of the 18 instruments were retrieved, with 2 of the 14 showing problems with the data that limit their use. The remaining 12 OBSs provided continuous, 19-month recordings from across a large part of the Northeast Atlantic seafloor.

Most SEA-SEIS stations were placed in the Irish Exclusive Economic Zone (EEZ), west of Ireland, and a few stations were placed in the EEZs of UK and Iceland (Fig. 1c). The deployment depths ranged from 1050 to 3930 m (Table 1).

All the broadband ocean bottom seismometers were NAMMU models, manufactured by K.U.M. Umwelt- und Meerestechnik Kiel GmbH (K.U.M., 2025). They were provided for the project by iMARL (the Insitu Marine Laboratory for Geosystems Research, https://imarl.ie), which is hosted by the Dublin Institute for Advanced Studies.

Each instrument was equipped with a 120-s, broadband Trillium Compact seismometer, manufactured by Nanometrics, Inc. (Nanometrics, Inc., 2025) and a hydrophone (model HTI-04-PCA/ULF) with frequency response of 0.01 Hz-8 kHz, manufactured by High Tech, Inc (High Tech, Inc., 2025). The K.U.M.'s KUMO 6D6 dataloggers recorded four channels, three for the seismic sensors (XYZ) and one for the hydrophone (H), using 32-bit resolution and obtaining 142 dB dynamic range. For the purposes of this paper, the horizontal component orientation codes are referred to by their original designations X and Y, rather than the more commonly-used codes 1 and 2. The OBS had a KUMQuat 562 releaser unit, which can receive acoustic signals down to a 6 km depth. The seismometer, the hydrophone, and the acoustic releaser are housed in an orange frame made of titanium and durable syntactic foam. Attached to the frame are a flag, a flasher (NOVATECH Mini-Flasher MMF-7500), and a radio beacon (NOVATECH Mini-Beacon 7500) (Fig. 2). The frame is connected to an anchor at its base by a hook, which can be rotated by the acoustic releaser once it receives an acoustic signal with the command to do so. An automated release mechanism is also present, which can release the hook at a preprogrammed time.

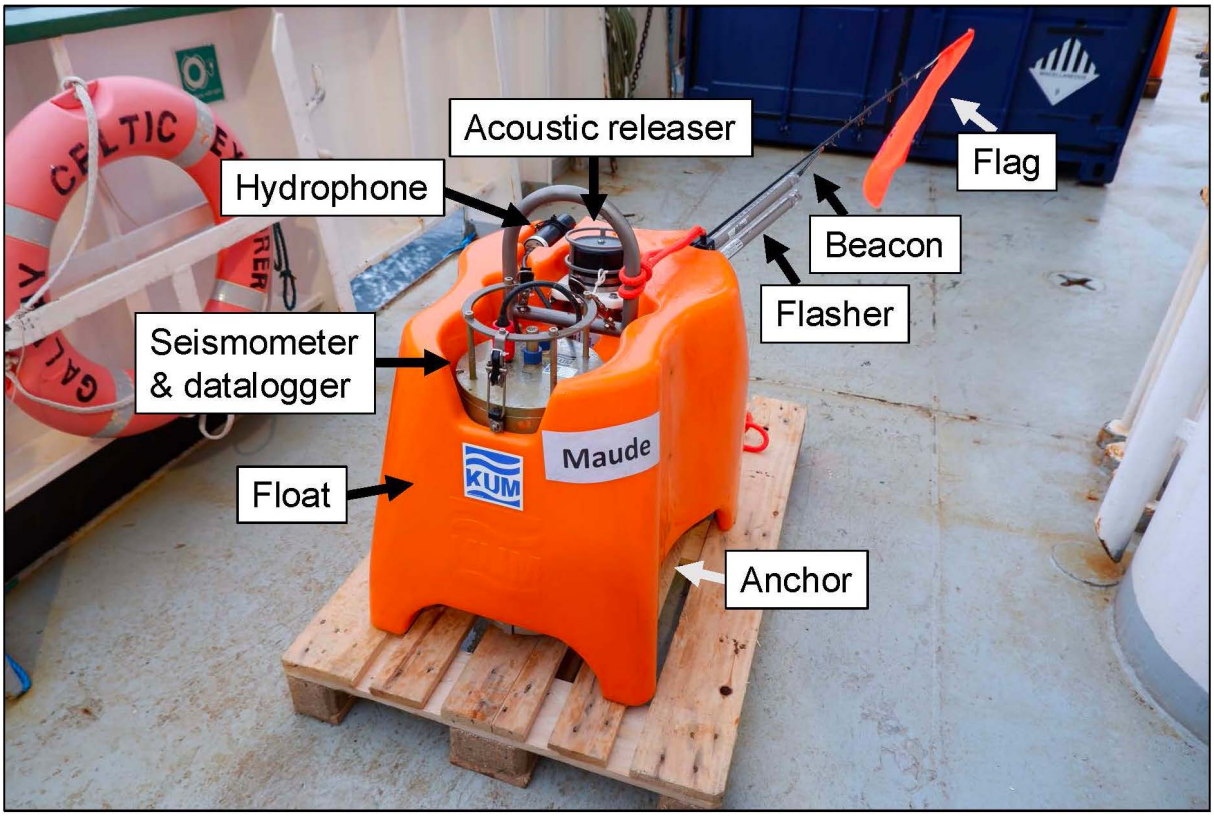

Figure 2. A NAMMU ocean bottom seismometer on board of the Celtic Explorer, after retrieval from the seafloor. To retrieve the NAMMU, the float has been detached from the anchor, which is left on the seafloor.

Table 1. Performance summary of the OBS experiment.

Station name	Latitude [°N]	Longitude [°E]	Triangulated [D/R*]	Depth [m]	Deployment date [UTC]	Retrieval date [UTC]	Recovered	End record [UTC]	Record length [days]	Skew value [s]
ALLOD	47.87791	−11.00766	YES [R]	3865	20/09/2018	10/05/2020	NO	—	—	—
BRIAN	49.84528	−13.97200	YES [R]	3930	21/09/2018	09/05/2020	YES	09/05/2020	596	−13.311
CHARL	58.80075	−15.49783	YES [D]	1150	24/09/2018	29/04/2020	YES	29/04/2020	583	−15.515
DUDE	61.445	−16.670	NO	2387	25/09/2018	02/05/2020	YES	02/05/2020	585	−21.330
EVE	50.89926	−13.09902	YES [R]	2157	21/09/2018	09/05/2020	YES	09/05/2020	596	−12.598
GILL	51.90051	−12.75105	YES [D&R]	1050	22/09/2018	08/05/2020	YES	08/05/2020	594	−13.390
GRAIN	54.47039	−14.78921	YES [R]	2750	23/09/2018	27/04/2020	YES	01/03/2020	525	+8.783
HARRY	57.90228	−12.10211	YES [D]	1745	24/09/2018	28/04/2020	NO	—	—	—
LIGEA	58.93944	−23.86983	YES [R]	2670	28/09/2018	03/05/2020	YES	03/05/2020	583	−10.702
LOCH	56.01132	−10.04166	YES [R]	2070	23/09/2018	28/04/2020	YES	28/04/2020	583	−20.397
LUIGI	59.525	−20.400	NO	2818	27/09/2018	01/05/2020	YES	01/05/2020	582	−11.786
MAUDE	52.475	−17.133	NO	3810	02/10/2018	07/05/2020	YES	07/05/2020	583	−13.181
NAMOR	61.50020	−22.05353	YES [D]	1794	26/09/2018	02/05/2020	YES	02/05/2020	584	−17.041
NEMO	57.02267	−18.50568	YES [D&R]	1250	30/09/2018	30/04/2020	NO	—	—	—
QUAKY	55.41990	−12.55907	YES [R]	2840	23/09/2018	27/04/2020	YES	27/04/2020	582	−7.553
SEBAS	54.13005	−19.83551	YES [D&R]	1310	01/10/2018	06/05/2020	NO	—	—	—
TOM	51.09948	−11.90448	YES [D&R]	1359	21/09/2018	08/05/2020	YES	08/05/2020	595	−11.089
WILSN	56.34345	−25.49841	YES [R]	3105	29/09/2018	04/05/2020	YES	04/05/2020	583	−12.785

* Triangulated on deployment [D] or recovery [R].

3. Deployment and Retrieval

The instruments were deployed by lifting them overboard with a crane and lowering them into the water. With the anchor attached, the OBS is negatively buoyant and sinks to the ocean bottom. Before deployment, the seismometer is turned on and synchronized with the GPS clock. A programmed automatic release date and time are set, in case the releaser fails to detach the OBS from the anchor following the receipt of the acoustic signal.

This date is generally a few months after the planned retrieval time, to provide time for securing extra retrieval ship time. The flasher and beacon are also turned on prior to the deployment. They deactivate once in the water and are meant to reactivate when back on the ocean surface.

To retrieve an instrument, an acoustic signal is sent to it from the ship. The acoustic releaser detects the signal and detaches the OBS from the anchor by rotating the hook that keeps them together by 90 degrees. Once the OBS is released from the anchor, it is positively buoyant and ascends at a ~0.9 m/s rate (based on the weight of the instrument). Once at the sea surface, the flasher and the beacon should reactivate. This facilitates spotting the instrument regardless of the time of day and weather. The OBS at the surface can also be spotted visually by its orange flag.

3.1 Triangulation

The location where the OBS is released from the ship can be measured accurately, but the instrument generally drifts laterally on its way to the seafloor due to ocean currents. The location of the OBS on the seafloor can be estimated through triangulation. For triangulation, an acoustic signal is sent down to the OBS and is returned by it. Assuming the acoustic wave speed in the seawater, the distance between the vessel and the OBS can be calculated from the two-way travel time. Using such measurements at multiple locations around the OBS, the location of the OBS can be accurately estimated.

Triangulation was performed on the OBS either just after deployment or just before the retrieval, or both, depending on the weather and time constraints. Triangulation was performed for all stations but three (MAUDE, DUDE, and LUIGI, Table 1). The drift, relative to the deployment position, turned out to be small (<200 m) in all cases. Therefore, for the three stations for which triangulation was not performed, we document the deployment coordinates, with the expectation that they are within ~200 m of the seafloor position.

3.2 Instrument retrieval: successes and problems

Of the 18 instruments deployed, 14 were retrieved successfully (plotted in green and orange in Fig. 1c). They detached from their anchors after receiving the acoustic release signal and surfaced after the expected time of the ascent, sufficiently close to the ship for their orange flags to be spotted. The instruments were brought on board, the seismometer clocks were synchronized with the GPS clock, and the data was harvested and stored.

The flasher and radio beacon did not work on any of the instruments and, thus, could not be used for nighttime retrievals. All the retrievals were therefore done in daylight. The flashers and beacons did resume working eventually, but could do so only once warm, clean and dry. The orange flags were the essential means of locating the seismometers from the ship.

Four of the instruments could not be retrieved (ALLOD, HARRY, NEMO, and SEBAS, labeled in red in Fig. 1c) and are still on the seafloor at the time of writing. These OBSs communicated with the ship as expected, but did not release from the anchor. In each case, we observed a lack of a delay in time between the OBS receiving the command and sending its confirmation signal. For successful retrievals, the OBS received the acoustic command, executed the detachment by rotating the hook, and then, after the execution, sent a confirmation signal, resulting in a few seconds delay. By contrast, this delay was absent in the failed attempts, suggesting that the command was acknowledged but not physically executed.

For these four instruments, a vessel was sent back to the locations of the OBSs at the pre-programmed automatic release time. Unfortunately, the OBS did not surface at the programmed time either. As before, the OBS could communicate with the ship but did not detach from the anchor. The only way to retrieve these instruments now would be by using a Remotely Operable Vehicle (ROV), which is logistically difficult and has not been possible so far.

The reason for the instruments' failure to detach remains unknown. One option is that the over-the-counter alkaline C-cell (baby) batteries that the release mechanisms were powered by drained over the 19 months of the deployment (though they should have a battery life of 24 months). The batteries provided enough power for the releaser to communicate with the ship, but may not have had enough power to rotate its hook. This, however, does not explain the failure of the pre-programmed automatic release, which is connected to a separate battery. Another option is that the instruments failed to release from the anchor due to a mechanical problem in the switchboard or the firmware.

4. Data

The SEA-SEIS experiment has delivered a unique broadband dataset, recorded by stations distributed across the Northeast Atlantic. The 4-channel recordings include continuous 3-component seismograms and hydrophone recordings, all at 250 samples per second. In this section, we report the instrumental problems, the data recovery rates, and the noise on the recorded data.

4.1 Instrumental problems

Two of the 14 retrieved OBSs had malfunctions in their seismometer recordings (DUDE and GRÁINNE, labeled orange in Fig. 1c). DUDE did not record the vertical component but, instead, recorded one of the horizontal components twice. The OBS thus recorded XYY data instead of XYZ data. GRÁINNE recorded very noisy data that are unusable for many purposes (Figs. A1-A3) and ran out of battery after just over 17 months (Table 2).

The poor quality of GRÁINNE's data was, possibly, due to a malfunction in the instrument's leveling procedure on the seafloor. The failure to level could explain the consumption of more battery power during its deployment: its continuous attempts to level may have drained the battery. A failure to level could be due to a stuck component in the instrument or an unstable position on the seafloor, perhaps due to a rough surface. Testing the instrument afterwards did not reveal any problems, suggesting the latter as a more plausible explanation.

4.2 Data recovery rates

Table 1 summarizes the deployment times, locations and other particulars of the stations of the network. The deployment of the instruments took 13 days from 20/09/2018 to 02/10/2018, and the retrieval took 14 days from 27/04/2020 to 10/5/2020. All stations thus spent 19 to 19.5 months on the seafloor (582 to 596 days). 13 of the 14 instruments recorded over the entire length of the deployment. Only GRÁINNE ran out of battery after 17 months (Section 4.1), recording 525 days of data.

In total, the data recovery was 8154 data days out of 10552 deployment days, which gives an overall rate of 77%. Excluding the OBSs that could not be retrieved, the data recovery rate is 99%.

4.3 Noise levels

Generally, the data quality of OBS is lower than that of land stations due to a higher noise level, especially at frequencies below 1Hz (e.g., Stähler et al., 2016; Janiszewski et al., 2023). This is also the case for the OBS data from this experiment. Figure 3 shows the probabilistic power spectral density (PPSD) plots of the vertical (HHZ), horizontal (HHX and HHY), and pressure (HDH) components of two of the instruments (BRIAN and NAMOR). The PPSD plots for all the instruments are given in the Appendix (Figs. A1-A4).

Compared to broadband land stations (which commonly have a noise spectrum between the grey lines in Fig. 3), the amplitude of the recorded signal of the OBSs is higher, especially at longer periods. The peak in amplitude between 1 to 10 s data is primarily due to the microseismic noise, while at longer periods (10-100 s), the net noise is dominated by the compliance and tilt noise (Section 5.3).

The amplitude of the signal in the PPSD plots, which characterizes the noise levels, varies per station. At 10-100 s, BRIAN has the lowest amplitude signal (lowest noise), and NAMOR has the highest (Fig. 3). BRIAN was deployed at one of the deepest locations, at 3930 m depth, while NAMOR was deployed in shallower water (1794 m deep). The shallower instruments are likely to experience higher noise levels due to waves and currents, whereas deeper instruments are usually in calmer conditions.

For all instruments, the horizontal components have a higher noise level than the vertical ones, especially at long periods (Fig. 3). This is similar to what has been observed in previous deployments both on land and on the seafloor (e.g., Stähler et al., 2016). The horizontal channels are more sensitive to ocean currents, causing tilting of the instrument, imperfections in its coupling to the seafloor, and the very low S wave velocities of the shallow sediments, all of which cause increased noise.

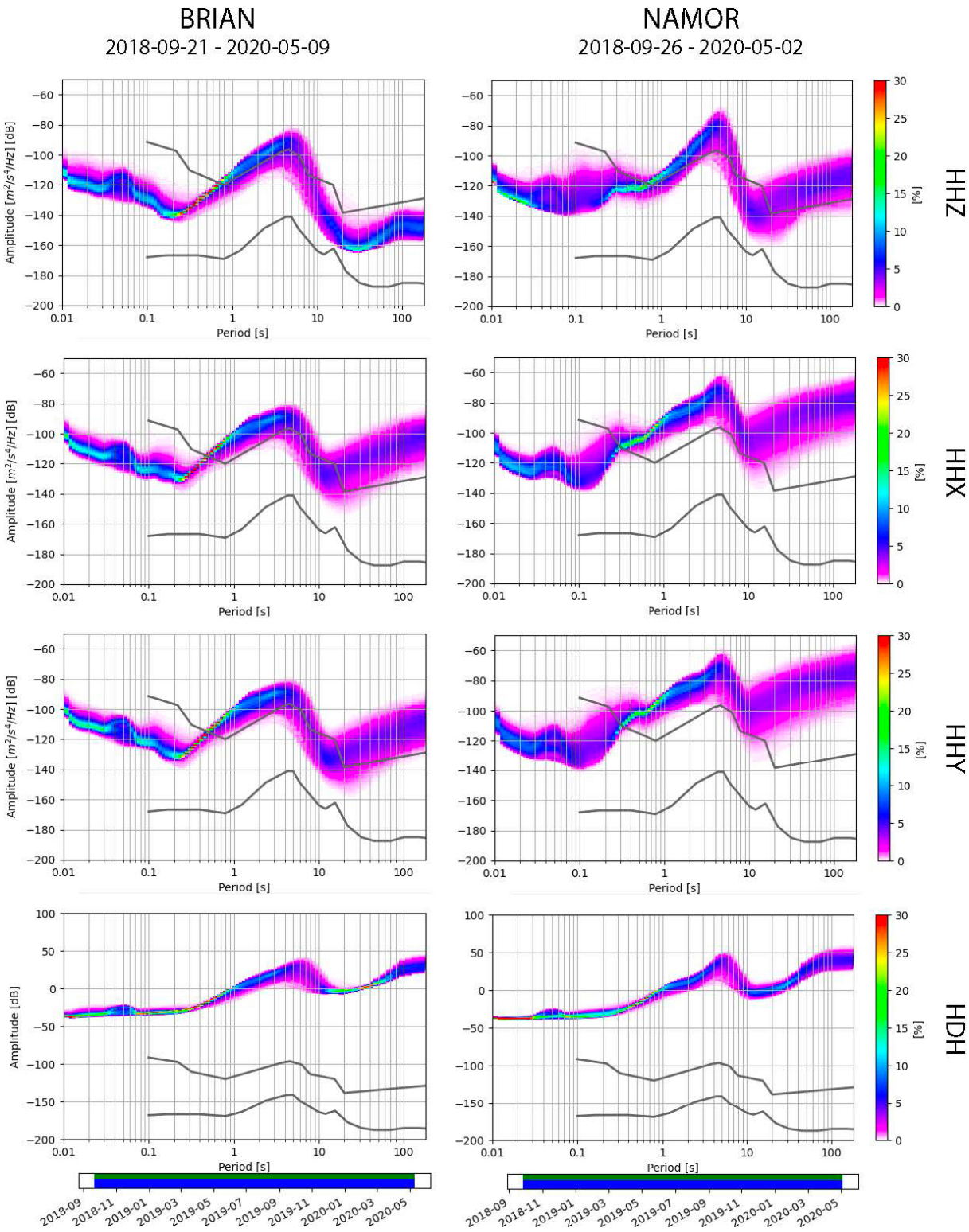

Figure 3. Probability power spectral density (PPSD) plots of the vertical (HHZ), horizontal (HHX and HHY) and hydrophone (HDH) components for two of the stations, BRIAN and NAMOR. BRIAN was one of the deepest deployments (3930 m depth), whereas NAMOR – one of the shallower ones (1794 m depth). The colours indicate the frequency of the occurrence of different noise levels from hour-long power spectra stacked over the time of the deployment. The red dashed lines indicate instrument self-noise for the Trillium Compact 120s. The grey lines mark the upper and lower bounds of the New High and Low Noise Model of Peterson (1993). Although these are not defined for hydrophone sensors, we include them in these panels for easy comparison to illustrate the difference in sensitivity between the components. The noise at BRIAN is lower than at NAMOR, probably due to its greater deployment depth.

5. Data pre-processing

5.1 Clock drift

One major limitation of OBSs, compared to land-based stations, is their inability to maintain accurate timing due to the lack of GPS-signal access underwater during their deployment. OBS instruments rely on internal clocks that tend to drift over time, making post-deployment clock drift correction a crucial step in processing the recorded data, especially for long-term deployments.

After the instrument is recovered and brought to the ship deck, the internal clock is synchronized with the GPS signal. The instrument-clock deviation from the true time, called the time skew, amounts to the total clock drift accumulated during the deployment. The skew is calculated and can be used to correct the data, assuming that the drift is linear over time. This assumption is not always valid, especially for long deployments (Gouédard et al., 2014; Hannemann et al., 2014; Hable et al., 2018). It is possible that the deployment or retrieval process, as well as varying environmental factors such as instrumental conditions, weather, or changes in temperature and pressure, could have induced non-linear clock drift.

According to GPS synchronization, the 12 successfully retrieved OBS units exhibited a time skew between −7 and −21 seconds (Table 1). The clock drift was assumed linear and corrected by linearly interpolating the time difference across the time interval of the deployment. Ambient noise cross-correlations were then used to verify the linearity assumption and ensure the accuracy of this correction.

Ambient noise cross-correlation analysis is a widely used method for clock drift correction (e.g., Sens-Schönfelder, 2008). It utilizes seismic noise, such as microseisms from ocean waves, continuously recorded by the OBSs. By cross-correlating this noise with data from nearby reference stations (either other OBS or land seismometers

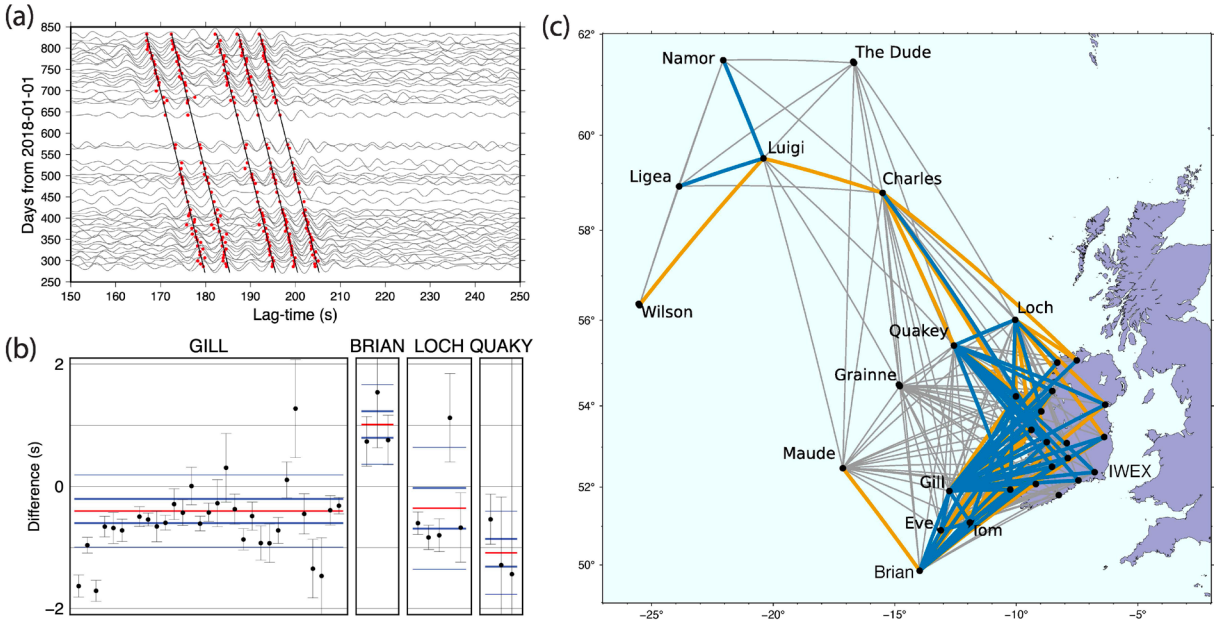

Figure 4. Analysis for the synchronization check of the OBS network using ambient noise cross-correlation. (a) time section of 1-hour-stacked daily cross-correlations for the station pair GILL (OBS) and IWEX (land station in Ireland, see panel (c) for location). The red dots represent the local maxima of the waveforms. The black lines show the estimated linear clock drift obtained by linear regression. (b) The estimation of the clock drift for the four OBSs for which it could be estimated with this method (GILL, BRIAN, LOCH, QUAKY). The black dots with error bars represent the estimates of the clock drift for that OBS station using different land stations (which have no clock drift by themselves). For each OBS, the average (red line), 1-sigma standard deviation (thick blue line), and 2-sigma standard deviation (thin/pale blue line) are shown. (c) Map view of pairs of stations for which cross-correlation measurements were performed. Blue lines: "good" pairs with robust measurements, orange lines: pairs with medium-quality measurements, grey lines: pairs with unusable cross-correlations. The location of land station IWEX in Ireland is marked.

with accurate clocks), timing discrepancies can be identified and used to correct the drift. This method offers advantages because it relies on passive noise sources, allowing continuous correction throughout the deployment. The time shift that maximizes the cross-correlation function reveals the drift, allowing us to compute a correction function (Sens-Schönfelder, 2008; Sabra et al., 2005; Gouédard et al., 2014; Hannemann et al., 2014; Stehly et al., 2007; Paul et al., 2005).

For the 12 OBS with readily usable vertical components, one-hour cross-correlation functions between the vertical components of seismograms of the OBS and nearby land stations in Ireland (Fig. 4c) were computed and stacked daily, with the (relative) maxima in the daily stacks analyzed to detect clock drift.

Due to the high noise level of the OBS, only four stations had a sufficient signal-to-noise ratio for a comprehensive drift analysis: GILL, BRIAN, LOCH, and QUAKY (Fig. 4b). The time skew estimated by this method matched the GPS synchronization results within error margins. For these stations, the drift is also almost exactly linear (e.g., Fig. 4a).

5.2 Obtaining horizontal component orientations

Since the OBSs fell freely through the water column to their positions on the seafloor, the orientations of the orthogonal horizontal components (HHX and HHY) for each station *in situ* are unknown. Knowledge of orientation is required for routine seismological techniques such as receiver functions and shear-wave splitting analysis. We constrain the orientations following the Doran-Laske-Orientation-Python (DLOPy) method of Doran and Laske (2017), using the observed particle motion of Rayleigh waves arriving at each station from global earthquakes. Rayleigh wave particle motion is elliptical in the vertical-radial plane, so observations allow one to infer the radial direction in the instrument's X-Y plane. Given that the expected radial direction is known from the great-circle path between the earthquake and the station, the geographical azimuths of the X and Y axes can be estimated.

The DLOPy method uses seven different frequency bands to calculate best fitting orientations, with central frequencies ranging from 10 mHz to 40 mHz in steps of 5 mHz, and with corner frequencies 5 mHz on either side of the central frequency. For each of these bands, a predicted arrival time of the Rayleigh wave is calculated using global dispersion maps (Ma et al., 2014; Ma and Masters, 2014), and a window is cut around the predicted arrival time. Doran and Laske (2017) found that different window lengths were optimal for different frequency bands, and we used the same window lengths as they did.

We use Rayleigh waves from all global earthquakes with magnitude >5.0 that occurred during the network deployment. We use both minor arc (R1) and major arc (R2) arrivals of Rayleigh waves (see Doran and Laske, 2017), resulting in up to fourteen values of the mean best fitting orientations ϕ (one for each frequency band for each of R1 and R2) per earthquake per station, and up to 6,160 per station in total. However, most of these measurements are dominated by noise. Following Doran and Laske (2017), we accept only those results with normalized cross-correlations, C_{zr}, >0.8. For example, in Fig. 5a, these values of ϕ cluster tightly around a mean orientation, whereas values with $C_{zr} < 0.8$ scatter more widely, representing noisier waveforms with a poorer constraint on orientation. Due to varying noise levels, the number of these accepted results differs significantly from station to station, from 28 at NAMOR to 401 at BRIAN (Table 2).

For all stations, we plot the calculated ϕ both as a function of Rayleigh wave back azimuth (Fig. 5c) and as a function of time (Fig. 5d), in order to check for systematic errors. No relationship with time can be observed, indicating that the instruments remained stationary throughout the deployment. A slight variation with backazimuth may be expected since Rayleigh waves can experience deviations in raypath due to heterogeneities in the Earth. Some instruments do record a slight anticlockwise shift in calculated orientation in the ~80-150° backazimuth range (e.g., BRIAN in Fig. 5c, LOCH, MAUDE and QUAKY), likely indicating some path bending due to structures in this direction.

In the case of LUIGI, however, at low frequencies (<25 mHz) spurious orientations with high C_{zr} are obtained for which ϕ directly correlates with backazimuth (Fig. B1c). This 1:1 relationship suggests the instrument is recording a unidirectional oscillation across the length of the deployment at these frequencies, mimicking a Rayleigh wave with a backazimuth of approximately 115°. We thus choose not to include any results from frequencies <25 mHz at LUIGI, and with only the higher frequency band, we find a stable mean orientation (Fig. B2).

We calculate the mean orientation and uncertainties following Doran and Laske (2017), automatically discarding outliers more than 5 times the Median Absolute Deviation from the median value, and using a bootstrap random sampling method. The uncertainties are given as twice the 95% confidence limit of the mean (i.e., 4σ, where

σ is the standard deviation of the means calculated for each bootstrap sample). This value is chosen to be conservative, in order to allow for systematic biases introduced by the uneven sampling of raypaths (Doran and Laske, 2017). We report orientations for all 12 stations that had no major issues (i.e., all retrieved stations but DUDE and GRÁINNE), with uncertainties ≤10°(Fig. 6, Table 2). Uncertainty tends to be lower for deeper instruments (Fig. 6b), likely reflecting lower noise levels, as was also inferred by Doran and Laske (2017).

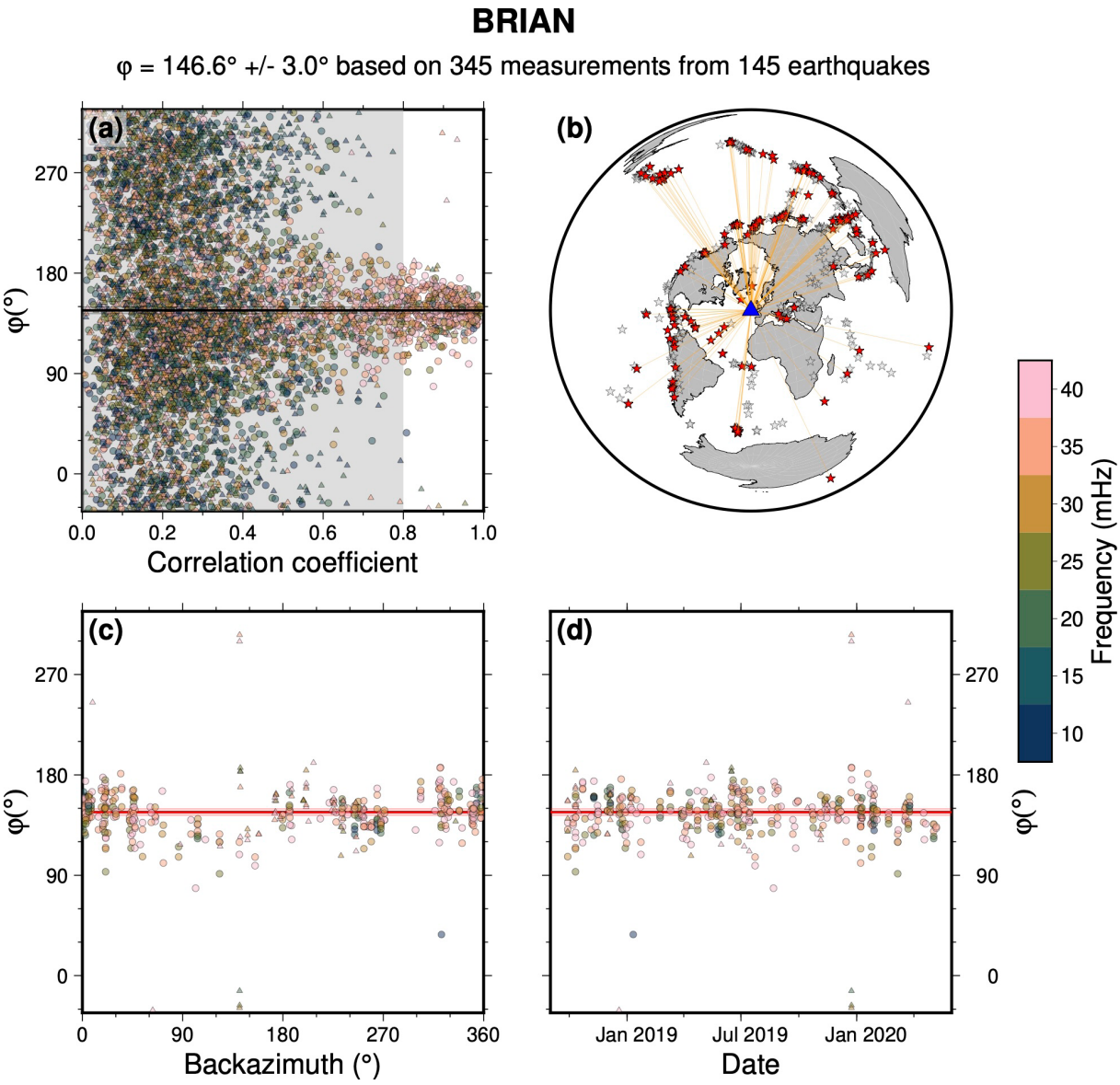

Figure 5. Determination of the orientation of the horizontal components for station BRIAN. (a) Best-fitting φ for all events and all frequencies used, plotted as a function of the normalized cross-correlation coefficient C_{zr}. Only the results with $C_{zr} > 0.8$ (unshaded region) are accepted. The thick black line and thin grey lines represent the mean and the standard error, respectively. (b) All earthquakes used, plotted as stars. Red stars are those that produced accepted results. The station location is marked by a blue triangle. (c) Accepted results plotted as a function of back azimuth. (d) Accepted results plotted as a function of time during the deployment. In panels (a), (c), and (d), the results are coloured by the central frequency of the filter band used, indicated by the colour scale on the right. Circles represent the R1 (minor arc) arrivals, and triangles represent the R2 (major arc) arrivals.

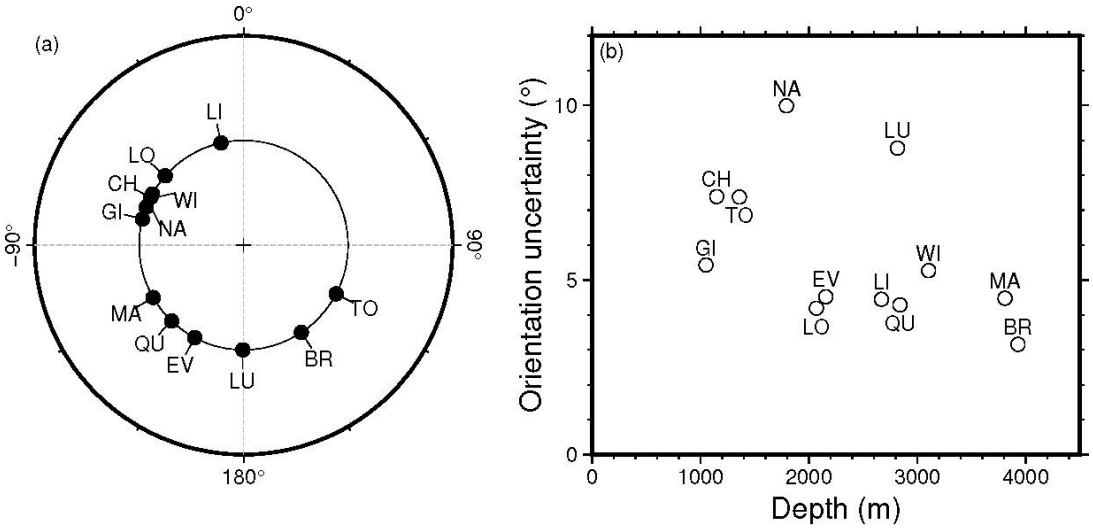

Figure 6. (a) Station orientations. (b) Orientation uncertainties, as defined by twice the 95% confidence limit, for all oriented stations, plotted as a function of water depth.

Table 2. Locations, depths and mean best fitting orientations (φ) of the HHY component of the 12 instruments (the HHX component is 90°clockwise of this). Uncertainties in φ are given by the 4σ value (twice the 95% confidence limit). Nmeas is the number of measurements used for each orientation (i.e., the number of measurements with $C_{zr} > 0.8$ for that station).

Station name	Latitude [°N]	Longitude [°E]	Depth [m]	φ (°)	4σ (°)	Nmeas
BRIAN	49.845	-13.972	3930	146.6	3.0	401
CHARL	58.801	-15.498	1150	297.3	8.0	77
EVE	50.899	-13.099	2157	209.0	4.1	213
GILL	51.901	-12.751	1050	286.6	5.5	109
LIGEA	58.939	-23.870	2670	347.6	4.3	49
LOCH	56.011	-10.042	2070	311.3	4.1	179
LUIGI	59.525	-20.400	2818	181.7	9.8	42
MAUDE	52.475	-17.133	3810	239.4	4.3	176
NAMOR	61.500	-22.053	1794	289.5	12.0	28
QUAKY	55.420	-12.559	2840	224.4	4.1	146
TOM	51.099	-11.904	1359	117.5	7.1	77
WILSN	56.343	-25.498	3105	297.2	6.2	65

5.3 Compliance and tilt noise removal for teleseismic events

At frequencies below 100 mHz, OBS data are strongly affected by the compliance and tilt noise (Webb and Crawford, 1999; Crawford and Webb, 2000; Bell et al., 2015). Compliance noise arises from the deformation of the seafloor under pressure changes caused by long-wavelength infragravity ocean waves at the water surface. Tilt noise can be caused by bottom currents exerting forces on the instrument.

Crawford and Webb (2000) developed a method to reduce the compliance and tilt noise on the vertical component using the transfer function of the pressure and horizontal components, respectively. Their approach to correct compliance noise is to calculate the frequency-dependent transfer function based on the spectral coherence between the pressure and vertical component of ambient seismic noise. This transfer function predicts the compliance noise in the vertical component by multiplying the pressure data by the transfer function. The compliance noise is then removed by subtracting it from the vertical component seismogram.

To remove tilt noise from the vertical component, the same approach is used as for the removal of the compliance noise, except that the transfer function is calculated based on the spectral coherence between the horizontal and vertical components of the ambient noise. The tilt noise is predicted by multiplying the horizontal data with the transfer function, and the predicted noise is then removed by subtracting it from the vertical component of the seismogram.

The module aTaCR (https://nfsi-canada.github.io/OBStools/atacr.html) uses the pressure and horizontal transfer functions to correct the vertical-component OBS recordings of teleseismic events for the compliance and tilt noise, respectively (Janiszewski et al., 2019). We applied aTaCR to the OBS data and calculated transfer functions per day, week, and month of the deployment. When using these various transfer functions to remove the compliance and tilt noise from the seismograms, we found that using the daily transfer functions gave us the best results. This is likely due to the variability in the noise in the Northeast Atlantic Ocean. Using the daily transfer functions, we successfully reduced the compliance and tilt noise on our vertical component teleseismic recordings (Fig. 7).

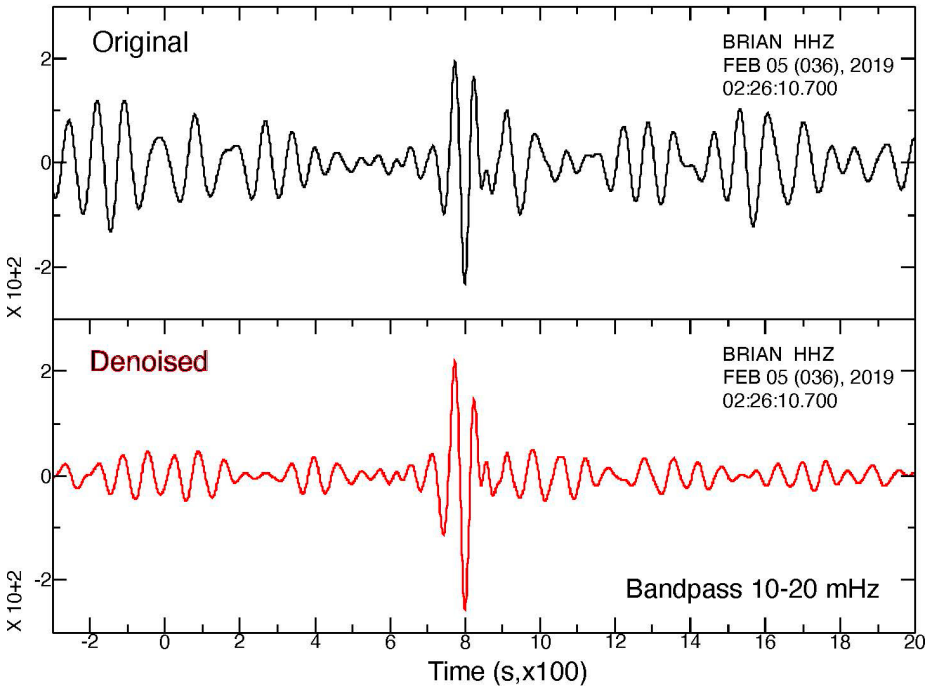

Figure 7. Vertical displacement seismograms of an earthquake M5.2 in Greece on 05/02/2019 recorded by station BRIAN, bandpass filtered at 10-20 mHz. Direct Rayleigh waves arrive at around 700-800 s, in the middle of the panels. Top: original seismogram. Bottom: seismogram after the removal of compliance and tilt noise using the aTaCR scheme (see Section 6.3).

6. Data examples

The SEA-SEIS stations recorded a variety of seismic and non-seismic signals. The dataset represents a valuable new resource for diverse geophysical, environmental, and marine-biology studies.

The stations of the SEA-SEIS network recorded numerous teleseismic earthquakes, providing high-quality seismograms, comparable to those recorded by nearby land-based stations. Figure 8 shows the waveform data from a Mw 7.5 earthquake that occurred on 25 May 2020, near the northern Kuril Trench. All 12 fully functional OBS stations, except for DUDE and GRÁINNE (which experienced technical issues, described in Section 4.1), successfully detected the first P-wave arrival. The comparison between the waveforms recorded by land stations in Ireland (in red) and the OBS stations (in blue) demonstrates the consistency of the seismic data, confirming reliability of the OBS network and the capability of OBSs to complement and enhance existing land-based seismic networks.

In addition to seismic events, the OBSs recorded various non-earthquake signals, creating potential for important interdisciplinary research. Figure 9a shows an hour-long vertical-component spectrogram recorded at LOCH at 10:00-11:00 on 23/09/2018. It reveals ship noise as a moving point source within the 20-50 Hz frequency range. This highlights the sensitivity of the OBSs to anthropogenic activity in the ocean.

The OBSs also recorded numerous fin whale and blue whale vocalizations. Figure 9b shows a vertical-component spectrogram recorded at LOCH, at 11:00-12.00 AM on 28/09/2018. It shows distinct short pulses in the 15-30 Hz range that fade in amplitude after approximately 30 minutes. These pulses are the recordings of the fin whale vocalizations (see Section 7 for a detailed image), matching the previously documented characteristics of fin whale calls (e.g., Pereira et al., 2020).

Whale vocalizations are the loudest biophonic sounds in the ocean and reach underwater sound pressure levels of up to 186 dB. They can be used for studying the whales' behavior, abundance and migration patterns (e.g., Zotter and Frank, 2019) and, possibly, even for seismic studies of the crust where conventional air-gun surveys are not available (Kuna and Nábelek, 2021).

The recordings of non-seismic signals in the SEA-SEIS data have significant scientific value. The in-situ recordings of the ship-generated noise characterize the acoustic pollution affecting marine mammals. The recordings of whale vocalizations will enable the identification and tracking of individual whales. It will also enable the studies of the abundance and migration patterns of the entire species, as well as the study of their communication systems. The abundance of signals of multiple origins in the SEA-SEIS data highlights the versatility of OBSs in supporting both geophysical and marine biology studies.

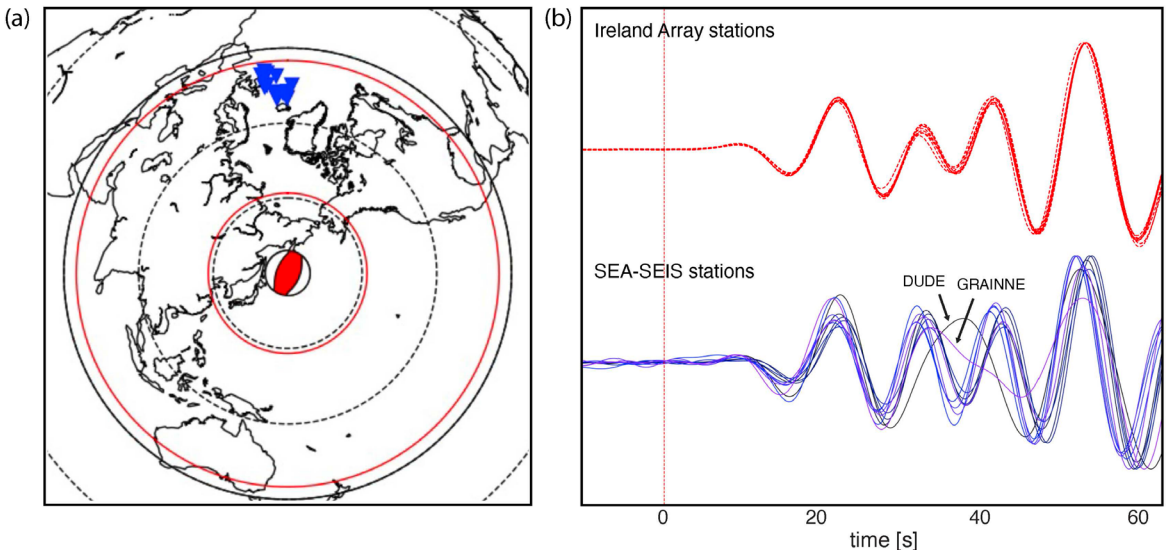

Figure 8. Seismograms of the Mw7.5 earthquake that occurred at 02:49:21 UTC on 25 May, 2020, near the northern Kuril Trench, southwest of the Kamchatka Peninsula (48.964°N, 157.696°E, 57.8 km depth). The recordings from the SEA-SEIS seismometers (blue, bottom) are compared with those from land stations in Ireland (red, top). Thevertical component traces are time drift- and response-corrected and plotted with a zoom on the long-period P waves. Time 0 is the P-wave arrival according to IASP91 (Kennett et al., 1995).

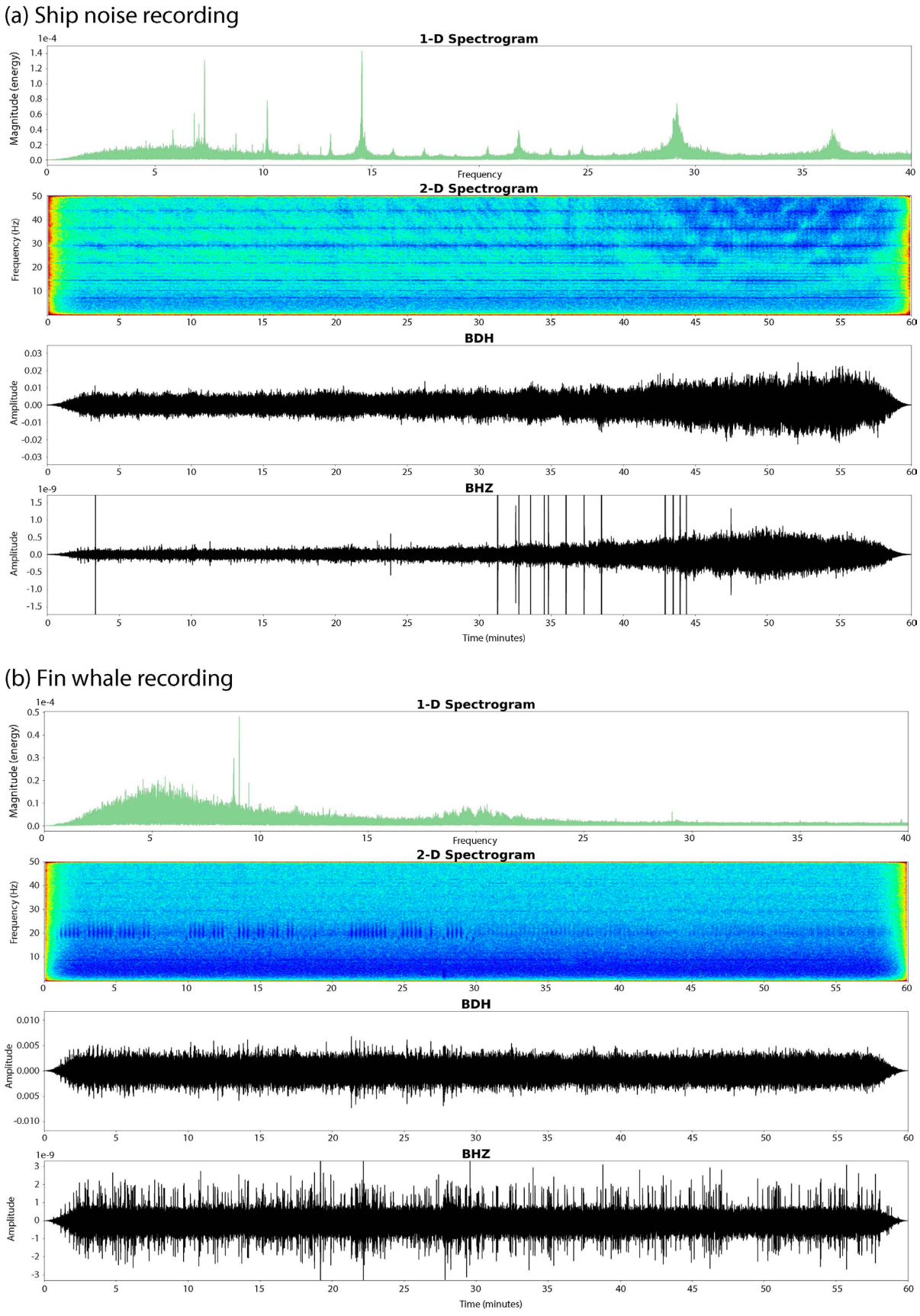

Figure 9. Seismic recording by LOCH of (a) a ship noise at 10:00-11.00 on 23/09/2018 and (b) a fin whale at 11:00-12.00 AM on 28/09/2018. Top to bottom: 1-D spectrogram of the recording giving the energy of the recording per frequency, 2-D spectrogram showing the amplitude of the signal per frequency range over time, recording of the BDH (hydrophone) channel over time, recording of the BHZ (vertical) channel over time.

7. Audification

The SEA-SEIS stations have recorded vibrations of the seafloor of diverse geophonic, biophonic and anthropophonic origins. We would normally not be able to hear most of these vibrations as sounds because their frequency range is below that audible by the human ear. Transforming and representing data in the audible frequency range is referred to as sonification. In sonification, the sounds may be edited and put in the form most suitable for a particular purpose, for example, for the detection of seismic events.

Audification, by contrast, is the direct translation of data waveforms to the audible frequency range, preserving the original characteristics of the data (e.g., Dean, 2009). In a multi-disciplinary effort comprising seismometry, signal processing and sound engineering, we have developed and applied new tools for audification, and applied them to SEA-SEIS and other seismic data.

Converting seismic signals to human-audible sound involves transforming seismic time-series data (at frequencies of 0.003 Hz up to 250 Hz) into frequencies within the range of human hearing (between 20 Hz and 20,000 Hz). The time scale of the seismogram gets compressed by accelerating it by a defined factor, shifting the frequency range upward into the audible range. Multiple types of normalization were developed, across different channels (including pressure), tailored to different analytical goals (seasonal variations, earthquakes, electronic noise, etc.) to ensure an effective conversion to sound (Figs. 10-11). While amplitude exaggeration can be used to highlight specific features, in this project, the fidelity to the original data is prioritized, avoiding any filtering, tapering, or signal manipulation. Additional frequency-shifting techniques were applied to bring all frequency components within the human hearing range.

By leveraging the spatial data captured by OBSs, ambisonic techniques create a spherical sound field from four components: omnidirectional pressure (hydrophone) and three directional velocity signals (seismometer). This allows the directionality of seismic and acoustic events – such as a ship's path or a whale's movement – to be perceived within the soundscape. Open-source audio tools (https://leomccormack.github.io/sparta-site/) were used to convert OBS channels into the first-order ambisonic format, enabling playback on multi-speaker arrays or headphones for an immersive listening experience. The audification and visualization of the data gave us a fresh perspective on the signals, from long-period current-induced vibrations to the microseisms, from teleseisms

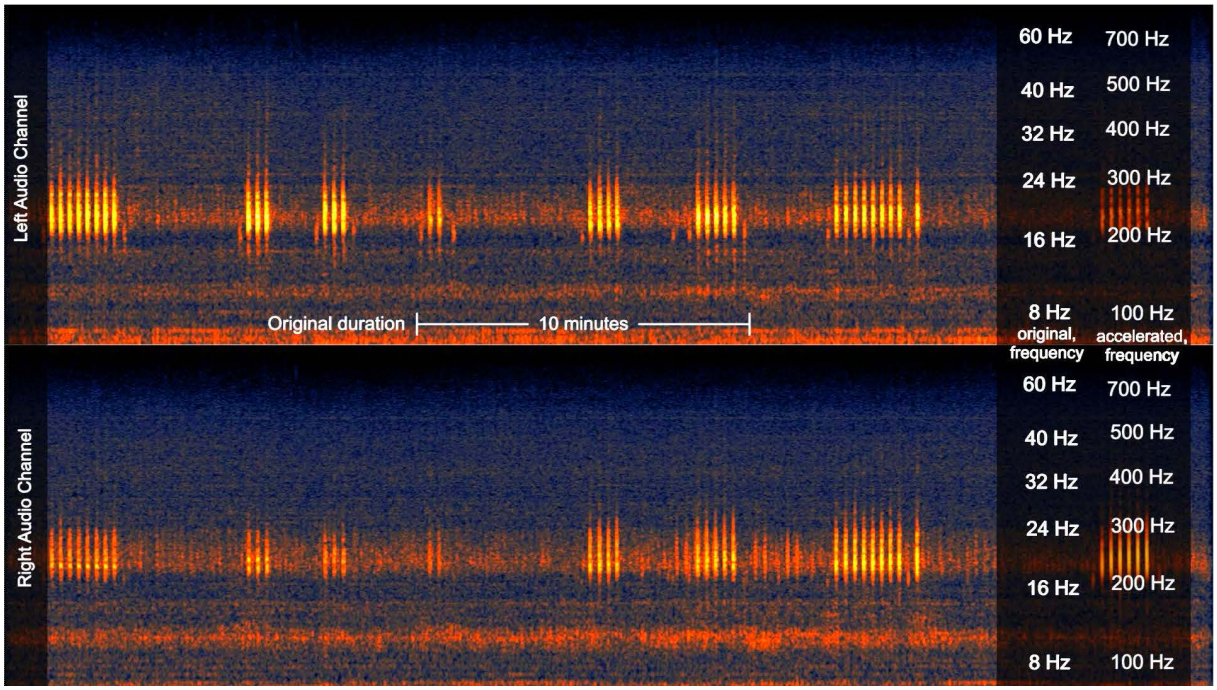

Figure 10. A stereo spectrogram of fin whale vocalizations, recorded by BRIAN, with the frequency content shifted by accelerating the seismogram to bring the vocalizations into human hearing range. The frequency range is given on the right, showing both the original (left) and the accelerated (right) frequency. The fin whale pulses are recorded primarily at 15-30 Hz and are transformed to 200-400 Hz to make them audible.

to regional earthquakes, and from whale vocalizations to ship traffic (Figs. 10-11). The audification also formed the basis for a productive, ongoing art-science collaboration (e.g., Sounds of the Earth, 2025).

Converting seismograms into audible sound is an effective method for education and public engagement (e.g., Dombois 2002; Holtzman et al., 2014; Jacobsen 2016; Lebedev et al., 2019). SEA-SEIS audifications were used in exhibitions, educational events and general-public shows. The methods developed are being applied to other seismic data as well.

The audifications of Earth-vibration data also offer unique material for original music composition. Examples of both new art and outreach material can be seen and listened to at Sounds of the Earth (2025).

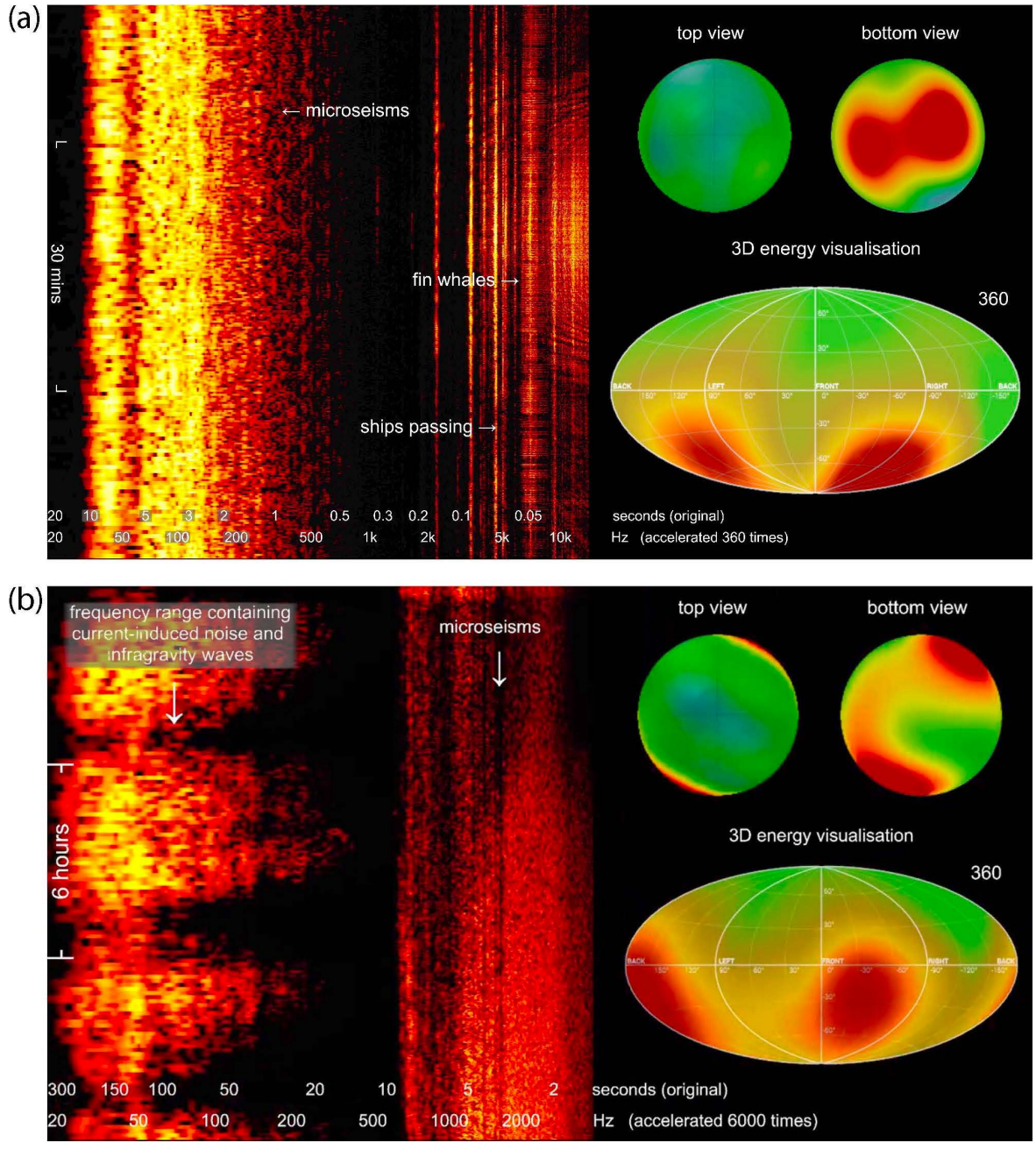

Figure 11. Visualization of one hour (top) and 18 hours (bottom) of seismic noise recorded by BRIAN on 19 April 2020, accelerated by a factor of 360 and 6000, respectively. Left: a spectogram showing amplitude of the signal over time at different frequencies. The different types of signal are labelled. The scales at the bottom are given in seconds (period) for the original signal, and in Hz for the accelerated signal. Right: 3D energy visualisation of the sonification of the seismic signal. Produced for the installation "The Earth Always Hums" (Sounds of the Earth, 2025).

8. Biological observations

Deep-sea biology was not on our mind when setting sail on our expeditions. But as we were getting our seismometers back from the seafloor, we found a variety of living creatures on them.

In effect, we performed a large-scale "growth experiment": 1) put metal-and-plastic structures on the seafloor at different locations over a vast area with a range of seafloor depths and geological and environmental settings; 2) leave in place for 19 months; 3) retrieve and examine what attached to them. We sampled locations across the deep-water Irish offshore territory, located to the west of Ireland, and some locations in the UK and Iceland waters (Fig. 1).

All the seismometers retrieved had marine organisms attached to them (Figs. 12, 13). Without going into marine biology in detail, our goal in this section is to document the observations, which represent new evidence on sea-creature habitats in the Northeast Atlantic Ocean.

The 1-4 km depth range below the surface of the ocean is known as the bathypelagic (or bathyal) zone. It is also called, colloquially, the Midnight Zone, as no sunlight penetrates here. There are no known plants there, because of the lack of light necessary for photosynthesis. All the creatures on our instruments were thus deep-sea animals, of a number of different species.

8.1 Octopusses

The largest sea creatures that came up on the seismometers were octopuses. They were found on the two seismometers deployed at the shallowest depths, Gill at ~1050 m depth in the Porcupine Basin and Charles at ~1150 m depth in the northern Hatton-Rockall Basin. GILL hosted two of them and CHARLES three, of which one detached from the instrument and dropped back into the sea as the OBS was being lifted onboard. All the octopuses looked very similar, apart from being somewhat different in size, and were probably of the same species. They were pale, light brown in color and had 40-50 cm long arms.

The octopuses had laid eggs on the plastic surfaces of both seismometers and were there guarding them. In one case, 20-30 eggs were on the outside wall of the structure. In all other cases, the eggs were laid in open cavities within or under the structure (Fig. 12). All the eggs looked similar: white, partly transparent, shaped like elongated pearls and rubbery on touch. They were 4-5 mm thick and 7-10 mm long, not counting the stem by which they were attached to the surfaces (Fig. 12). Black tar-like substance, likely to be the octopus ink, was deposited on the surfaces that the eggs were attached to. The long rope folded within one of the OBSs just beneath one of the nests on GILL was covered with this black ink (Fig. 12).

At the deeper sites in the Porcupine Basin-Tom at 1360 m depth and Eve at 2160 m depth-there were no octopuses or octopus eggs, and neither were there any at the deeper sites in the Hatton-Rockall Basin (Loch Ness Mometer, 2070 m; Quakey, 2840 m; Gráinne, 2750 m). We can infer that these octopuses' habitat extends to depths shallower than ~2000 m – possibly, only up to about 1200 m.

The deep seafloor is largely flat and featureless. The seismometers must have presented the animals with attractive options for nesting. Little is known about the octopus spawning habitat, and these new observations are scientifically useful and interesting. In particular, we can infer that the octopuses sought hard structures to lay their eggs on, which has been suspected but not proven and may have important conservation implications (Louise Allcock, pers. comm., 2020).

Figure 12. Octopuses and octopus eggs found on GILL and CHARLES after the retrieval of the instruments from the seafloor.

8.2 Other organisms

The number of organisms attached to the OBS generally decreased with the deployment depth. All instruments had sea creatures on them (Figs. 12-13). This allowed us to sample the entire 1-4 km depth range. Additionally, a variation in the type and amount of organisms on the OBS was observed with the location of the instrument. The most remote stations (NAMOR, DUDE, LUIGI and LIGEA) had the least amount and variation of sea-organisms attached (Fig. 13).

The different types of organisms preferred different materials to attach themselves to. While some organisms were mostly observed on the titanium of the flasher and the beacon or the rubber of the flag, others only attached themselves to the foam of the float (Figs. 12-13).

The small organisms are not straightforward to identify. The observations, however, may be of value to specialists. We thus document our observations using the photographs taken immediately after the OBS came on board (Figs. 12-13).

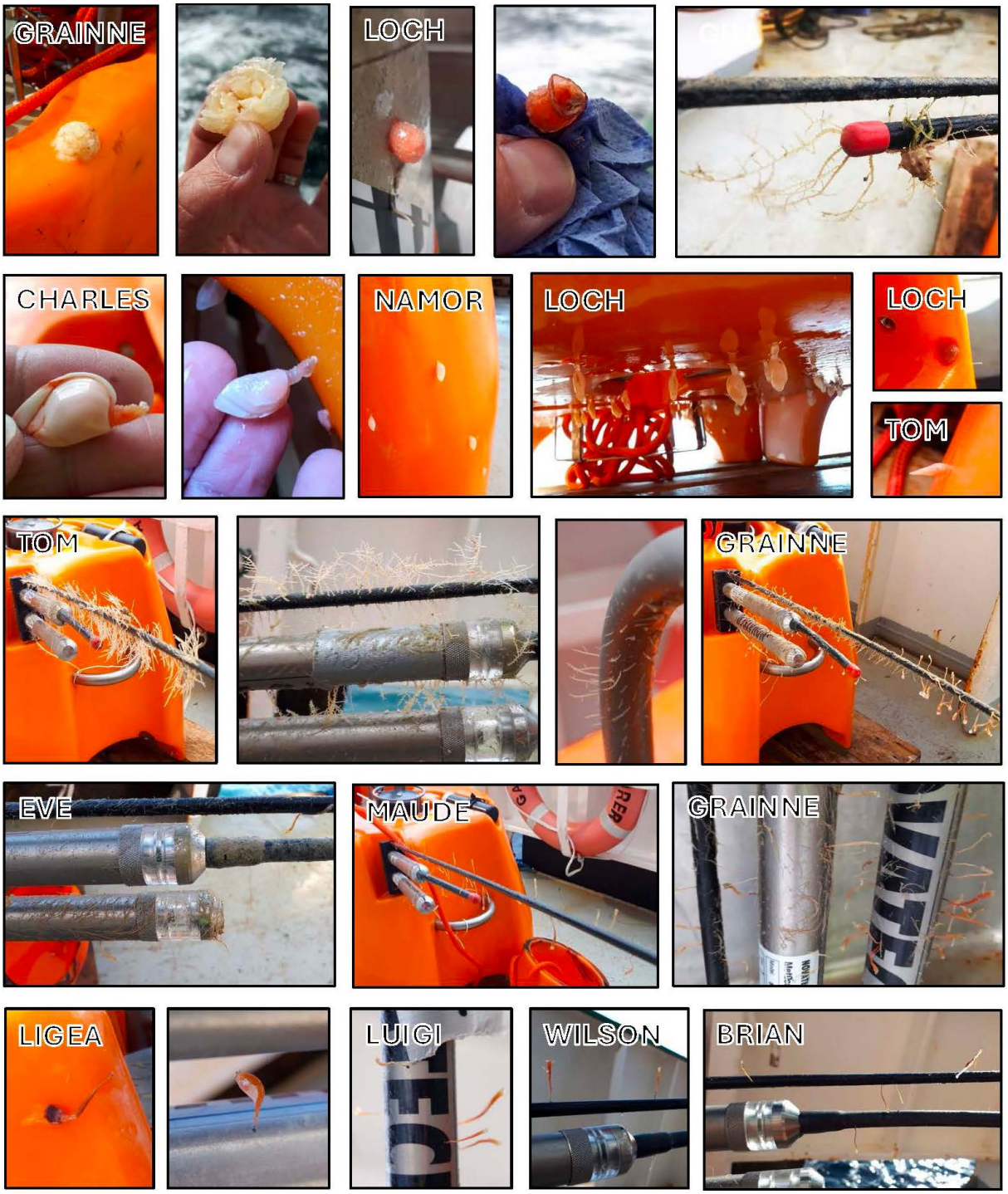

Figure 13. Sea creatures found on the OBSs after their retrieval from the seafloor. Some organisms were attached to the metal flasher, beacon and flag, whereas others preferred to attach to the plastic float (orange).

9. Conclusions

The project SEA-SEIS has recorded unique broadband seismic and acoustic data from across a large part of the Northeast Atlantic Ocean. The network recorded 3-component seismic data and hydrophone data continuously for 19 months. Fourteen of the 18 instruments were retrieved from the seafloor. Quality control and pre-processing showed that 12 seismometers recorded high-quality seismic data for the entire duration, with different problems at the remaining two seismometers.

The data contains high-quality recordings of numerous teleseismic and regional earthquakes and a broad range of other geophonic, biophonic, and anthropophonic signals. Linear clock drift correction was performed, and the ambient-noise cross-correlation analysis for some of the stations confirmed the linear-correction accuracy. The orientation of the horizontal component was determined using teleseismic Rayleigh wave arrivals. The compliance and tilt noise in vertical-component, teleseismic event data was reduced using the pressure and horizontal transfer functions.

All instruments came back onboard with different species of sea creatures attached to them, including octopuses for shallower deployments and smaller organisms elsewhere. In addition to their main purpose, OBS deployments can yield important information on the habitats of different species, with important conservation implications.

New methods developed for the audification of the seismic and hydrophone data transform the spatial information contained within the data to ambisonic surround sound. The audification offers new perspectives on the data and is an effective means of communicating science to broad audiences. It also forms the basis for productive art-science collaborations.

Data availability statement. The SEA-SEIS data are archived and will be distributed via FDSN, http://fdsn.fdsn.org/networks/detail/4R_2018. The data are scheduled for a 2025 release following the iMARL (the Insitu Marine Laboratory for Geosystems Research, https://imarl.ie) policies.

Acknowledgements. The manuscript has benefitted from constructive feedback from the editor Petr Kolínský and two anonymous reviewers. The ocean-bottom seismometers for SEA-SEIS were provided by iMARL, the Insitu Marine Laboratory for Geosystems Research hosted by DIAS (https://imarl.ie, last accessed January, 2025). The RV Celtic Explorer is run by the Marine Institute (https://www.marine.ie, last accessed January, 2025). We are grateful to Captain Denis Rowan, the crew of the RV Celtic Explorer, and Aodhán Fitzgerald, Research Vessel Operations Manager, Marine Institute, for their expert assistance in achieving the scientific and outreach objectives of the SEA-SEIS research cruises. We thank Arne Schwenk from K.U.M., who joined us on the OBS deployment expedition and provided expert guidance. We are grateful to Louise Allcock for marine biology discussion and information. The SEA-SEIS project was co-funded by the Science Foundation Ireland, the Geological Survey of Ireland, and the Marine Institute (grant 16/IA/4598). We acknowledge additional support from the UK Natural Environment Research Council Grants NE/X000060/1 and NE/Y000218/1, Project InnerSpace (https://projectinnerspace.org, last accessed January, 2025) and the project 4D Dynamic Earth, funded by ESA (4000140327/23/NL/SD) as part of EXPRO+.

References

Agius, M. R., N. Harmon, C. A. Rychert, S. Tharimena and J. M. Kendall (2018). Sediment characterization at the equatorial Mid-Atlantic Ridge from P-to-S teleseismic phase conversions recorded on the PI-LAB experiment, Geophys. Res. Lett., 45, 12244-12252, doi:10.1029/2018GL080565.

Barcheck, G., G. Abers, A. Adams, A. Bécel, J. Collins et al. (2020). The Alaska amphibious community seismic experiment, Seismol. Res. Lett., 91, 3054-3063, doi:10.1785/0220200189.

Barreyre, T., L. Ottemöller, V. Schlindwein, R. B. Pedersen and M. Schmidt-Aursch (2023). Project LOKI: DEPAS ocean-bottom seismometer operations at Loki's Castle vent field in 2019-2020, GFZ Data Services, Dataset/Seismic Network, doi:10.14470/3Z326135.

Beauduin, R. and J. P. Montagney (1996). Time evolution of broadband seismic noise during the French pilot experiment OFM/SISMOBS, Geophys. Res. Lett., 23, 2995-2998, doi:10.1029/96GL02880.

Bell, S., D. Forsyth and Y. Ruan (2015). Removing noise from the vertical component records of ocean-bottom seismometers: Results from year one of the Cascadia Initiative, Bull. Seismol. Soc. Am., 105, 300-313, doi:10.1785/0120140054.

Bensen, G., M. Ritzwoller, M. Barmin, A. Levshin, F. Lin et al. (2007). Processing seismic ambient noise data to obtain reliable broad-band surface wave dispersion measurements, Geophys. J. Int., 169, 1239-1260, doi:10.1111/j.1365-246X.2007.03374.x.

Bonadio, R., W. H. Geissler, S. Lebedev, J. Fullea, M. Ravenna et al. (2018). Hot upper mantle beneath the Tristan da Cunha hotspot from probabilistic Rayleigh-wave inversion and petrological modeling, Geochem. Geophys. Geosyst., 19, 1412-1428, doi:10.1002/2017GC007347.

Collins, J. A., F. L. Vernon, J. A. Orcutt, R. A. Stephen, K. R. Peal et al. (2001). Broadband seismology in the oceans: Lessons from the ocean seismic network pilot experiment, Geophys. Res. Lett., 28, 49-52, doi:10.1029/2000GL011638.

Craig, D., C. Bean and F. LePape (2019). Microseism sources observed with seismic arrays and an OBS network in Ireland, in Geophys. Res. Abstr., 21.

Crawford, W. and S. Webb (2000). Identifying and removing tilt noise from low-frequency (<0.1 Hz) seafloor vertical seismic data, Bull. Seismol. Soc. Am., 90, 952-963, doi:10.1785/0119990121.

Czuba, W., M. Grad, R. Mjelde, A. Guterch, A. Libak et al. (2010). Continent-ocean transition across a trans-tensional margin segment: off Bear Island, Barents Sea, Geophys. J. Int., 184, 541-554, doi:10.1111/j.1365-246X.2010.04873.x.

Dahm, T., F. Tilmann and J. P. Morgan (2006). Seismic broadband ocean-bottom data and noise observed with free-fall stations: Experiences from long-term deployments in the North Atlantic and the Tyrrhenian Sea, Bull. Seismol. Soc. Am., 96, 647-664, doi:10.1785/0120040064.

Dean, R. (2009). The Oxford Handbook of Computer Music, Oxford University Press, New York, 321 pp., ISSN:9780195331615, doi:10.1093/oxfordhb/9780199792030.001.0001.

Dombois, F. (2002). Auditory seismology on free oscillations, focal mechanisms, explosions and synthetic seismograms, in Proc. 8th Int. Conf. Auditory Display, 27-30.

Doran, A. and G. Laske (2017). Ocean-bottom seismometer instrument orientations via automated Rayleigh-wave arrival-angle measurements, Bull. Seismol. Soc. Am., 107, 691-708, doi:10.1785/0120160165.

Geissler, W. H., W. Jokat, M. Jegen and K. Baba (2017). Thickness of the oceanic crust, the lithosphere, and the mantle transition zone in the vicinity of the Tristan da Cunha hot spot estimated from ocean-bottom and ocean-island seismometer receiver functions, Tectonophysics, 716, 33-51, doi:10.1016/j.tecto.2016.12.013.

Gouédard, P., T. Seher, J. McGuire, J. Collins and R. van der Hilst (2014). Correction of ocean-bottom seismometer instrumental clock errors using ambient seismic noise, Bull. Seismol. Soc. Am., 104, 1276-1288, doi:10.1785/0120130157.

Hable, S., K. Sigloch, G. Barruol, S. Stähler and C. Hadziioannou (2018). Clock errors in land and ocean bottom seismograms: High-accuracy estimates from multiple-component noise cross-correlations, Geophys. J. Int., 214, 2014-2034, doi:10.1093/gji/ggy236.

Hannemann, K., F. Krüger and T. Dahm (2014). Measuring of clock drift rates and static time offsets of ocean bottom stations by means of ambient noise, Geophys. J. Int., 196, 1034-1042, doi:10.1093/gji/ggt434.

Harmon, N., C. A. Rychert, J. M. Kendall, M. Agius, P. Bogiatzis et al. (2020). Evolution of the oceanic lithosphere in the equatorial Atlantic from Rayleigh wave tomography, evidence for small-scale convection from the PI-LAB experiment, Geochem. Geophys. Geosyst., 21, e2020GC009174, doi:10.1029/2020GC009174.

Holtzman, B., J. Candler, M. Turk and D. Peter (2014). Seismic sound lab: Sights, sounds and perception of the earth as an acoustic space, in Sound, Music, and Motion: 10th Int. Symp. CMMR 2013, Marseille, France, Springer, 161-174, doi:10.1007/978-3-319-12976-1_10.

Jacobsen, E. (2016). Seismic wave videos combine sight and sound, Eos, Trans. Am. Geophys. Union, 97, doi:10.1029/2016EO060261.

Janiszewski, H., J. Gaherty, G. Abers, H. Gao and Z. Eilon (2019). Amphibious surface-wave phase-velocity measurements of the Cascadia subduction zone, Geophys. J. Int., 217, 1929-1948, doi:10.1093/gji/ggz051.

Janiszewski, H. A., Z. Eilon, J. B. Russell, B. Brunsvik, J. B. Gaherty et al. (2023). Broad-band ocean bottom seismometer noise properties, Geophys. J. Int., 233, 297-315, doi:10.1093/gji/ggac450.

Jeddi, Z., L. Ottemöller, M. Sørensen, S. Rezaei, S. Gibbons et al. (2021). Improved seismic monitoring with OBS deployment in the Arctic: A pilot study from offshore western Svalbard, Seismol. Res. Lett., 92, 2705-2717, doi:10.1785/0220200471.

Kennett, B., E. Engdahl and R. Buland (1995). Constraints on seismic velocities in the Earth from traveltimes, Geophys. J. Int., 122, 108-124, doi:10.1111/j.1365-246X.1995.tb03540.x.

Kuna, V. and J. Nábělek (2021). Seismic crustal imaging using fin whale songs, Science, 371, 731-735, doi:10.1126/science.abf3962.

Laske, G., J. A. Collins, C. J. Wolfe, S. C. Solomon, R. S. Detrick et al. (2009). Probing the Hawaiian hot spot with new broadband ocean bottom instruments, Eos, Trans. Am. Geophys. Union, 90, 362-363, doi:10.1029/2009EO410002.

Lebedev, S., R. Bonadio, C. Gómez-García, J. I. de Laat, L. Bérdi et al. (2019). Education and public engagement using an active research project: lessons and recipes from the SEA-SEIS North Atlantic Expedition's programme for Irish schools, Geosci. Commun., 2, 143-155, doi:10.5194/gc-2-143-2019.

Ma, Z. and G. Masters (2014). A new global Rayleigh- and Love-wave group velocity dataset for constraining lithosphere properties, Bull. Seismol. Soc. Am., 104, 2007-2026, doi:10.1785/0120130320.

Ma, Z., G. Masters, G. Laske and M. Pasyanos (2014). A comprehensive dispersion model of surface wave phase and group velocity for the globe, Geophys. J. Int., 199, 113-135, doi:10.1093/gji/ggu246.

Parisi, L., N. Augustin, D. Trippanera, H. Kirk, A. Dannowski et al. (2024). The first network of ocean bottom seismometers in the Red Sea to investigate the Zabargad Fracture Zone, Seismica, 3, 1-21, doi:10.26443/seismica.v3i1.729.

Paul, A., M. Campillo, L. Margerin, E. Larose and A. Derode (2005). Empirical synthesis of time-asymmetrical Green functions from the correlation of coda waves, J. Geophys. Res., 110, B08302, doi:10.1029/2004JB003521.

Pereira, A., D. Harris, P. Tyack and L. Matias (2020). Fin whale acoustic presence and song characteristics in seas to the southwest of Portugal, J. Acoust. Soc. Am., 147, 2235-2249, doi:10.1121/10.0001066.

Peterson, J. R. (1993). Observations and modeling of seismic background noise, US Geological Survey, Technical Report, doi:10.3133/ofr93322.

Sabra, K., P. Roux, A. Thode, G. D'Spain, W. Hodgkiss and W. Kuperman (2005). Using ocean ambient noise for array self-localization and self-synchronization, IEEE J. Oceanic Eng., 30, 338-347, doi:10.1109/JOE.2005.850908.

Sens-Schönfelder, C. (2008). Synchronizing seismic networks with ambient noise, Geophys. J. Int., 174, 966-970, doi:10.1111/j.1365-246X.2008.03842.x.

Stähler, S., K. Sigloch, K. Hosseini, W. Crawford, G. Barruol et al. (2016). Performance report of the RHUM-RUM ocean bottom seismometer network around La Réunion, western Indian Ocean, Adv. Geosci., 41, 43-63, doi:10.5194/adgeo-41-43-2016.

Stehly, L., M. Campillo and N. Shapiro (2007). Traveltime measurements from noise correlation: stability and detection of instrumental time-shifts, Geophys. J. Int., 171, 223-230, doi:10.1111/j.1365-246X.2007.03492.x.

Suyehiro, K., T. Kanazawa, N. Hirata, M. Shinohara and H. Kinoshita (1992). Broadband downhole digital seismometer experiment at site 794: a technical paper, Ocean Drilling Program, 1061-1073.

Tsekhmistrenko, M., K. Sigloch, K. Hosseini and G. Barruol (2021). A tree of Indo-African mantle plumes imaged by seismic tomography, Nat. Geosci., 14, 612-619, doi:10.1038/s41561-021-00762-9.

Tsekhmistrenko, M., A. Ferreira, M. Miranda, S. Baranbooei, R. Cabieces Diaz et al. (submitted). Performance of the 2021-2022 UPFLOW large ocean bottom seismometer array in the Azores-Madeira-Canary Islands region, Atlantic Ocean, Seismica.

Webb, S. C. and W. C. Crawford (1999). Long-period seafloor seismology and deformation under ocean waves, Bull. Seismol. Soc. Am., 89, 1535-1542, doi:10.1785/BSSA0890061535.

Yang, Z., A. Sheehan, J. Collins and G. Laske (2012). The character of seafloor ambient noise recorded offshore New Zealand: Results from the MOANA ocean bottom seismic experiment, Geochem. Geophys. Geosyst., 13, doi:10.1029/2012GC004201.

Zotter, F. and M. Frank (2019). Ambisonics: A practical 3D audio theory for recording, studio production, sound reinforcement, and virtual reality, Springer Nature, doi:10.1007/978-3-030-17207-7.

Appendix A. PPSD plots

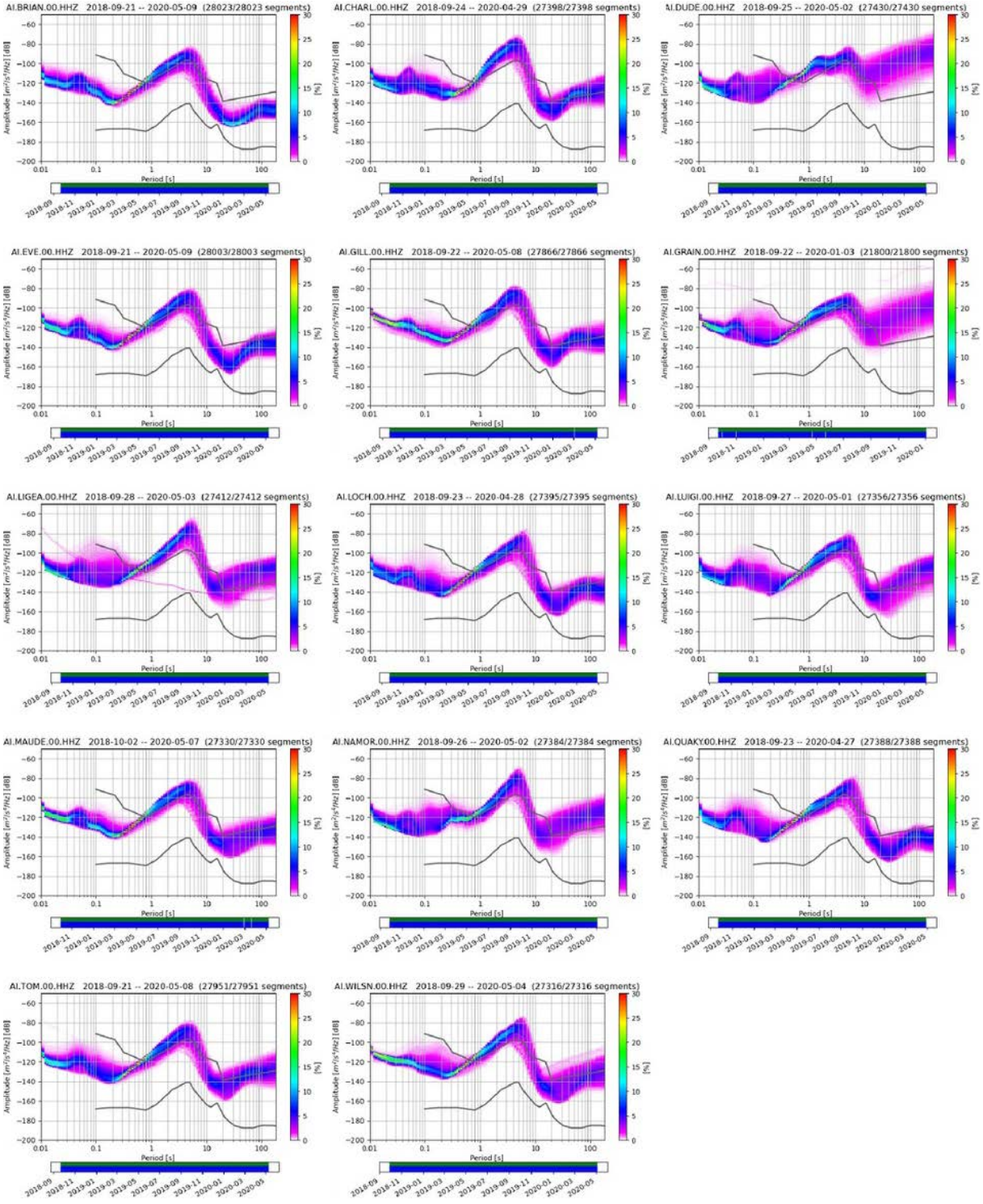

Figure A1. Probability power spectral density (PPSD) plots of the Z component of the 14 OBSs retrieved.

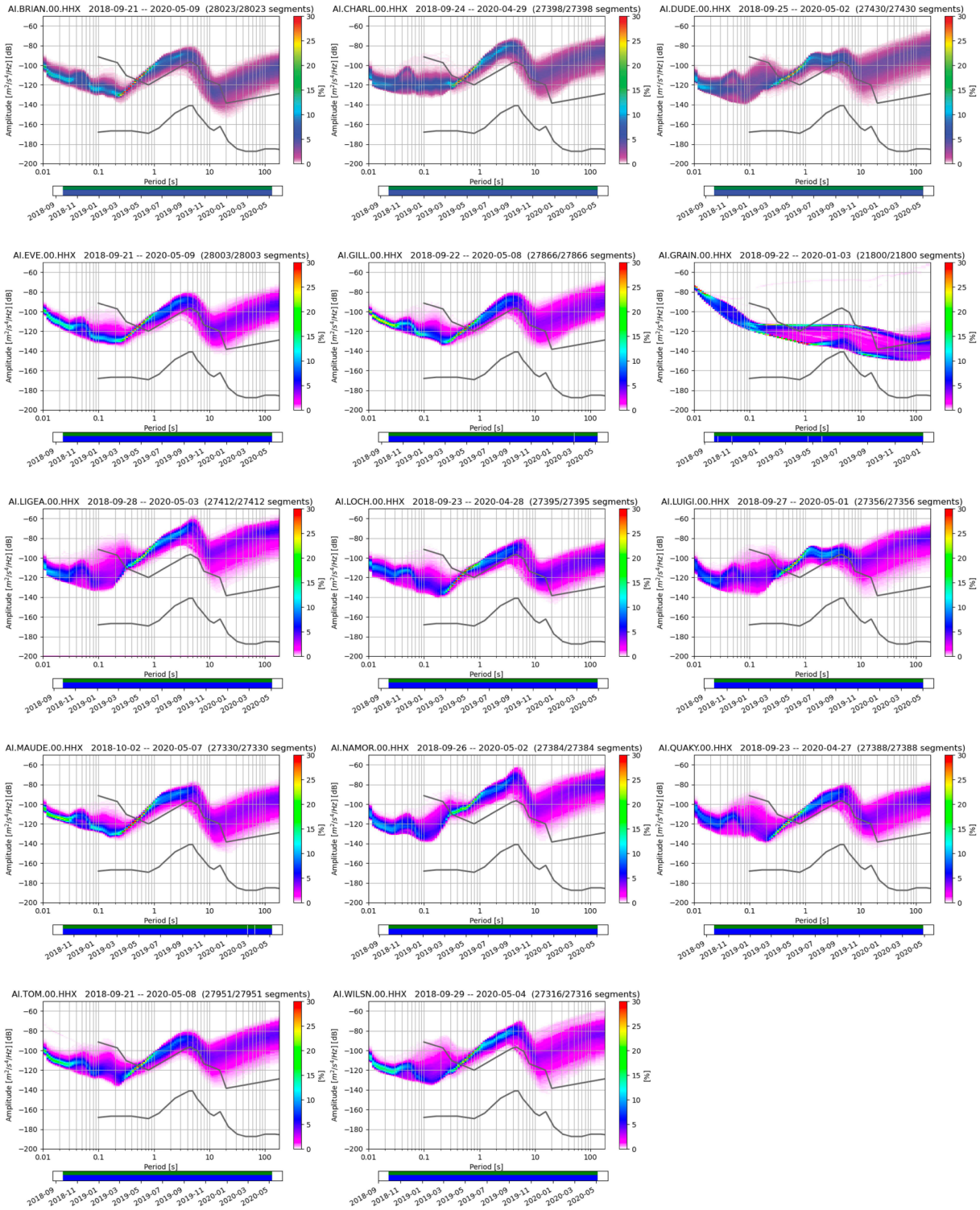

Figure A2. Probability power spectral density (PPSD) plots of the X component of the 14 OBSs retrieved.

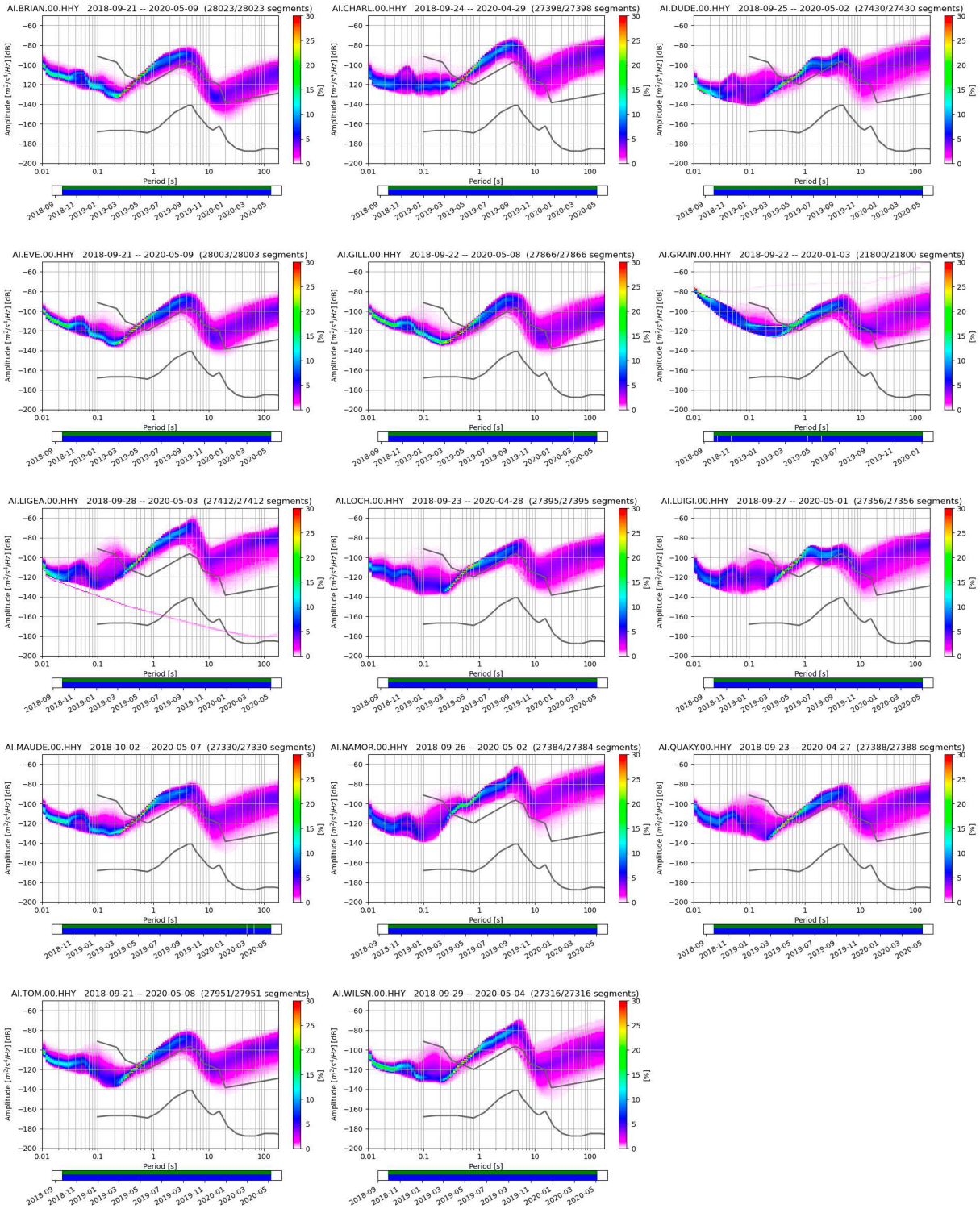

Figure A3. Probability power spectral density (PPSD) plots of the Y component of the 14 OBSs retrieved.

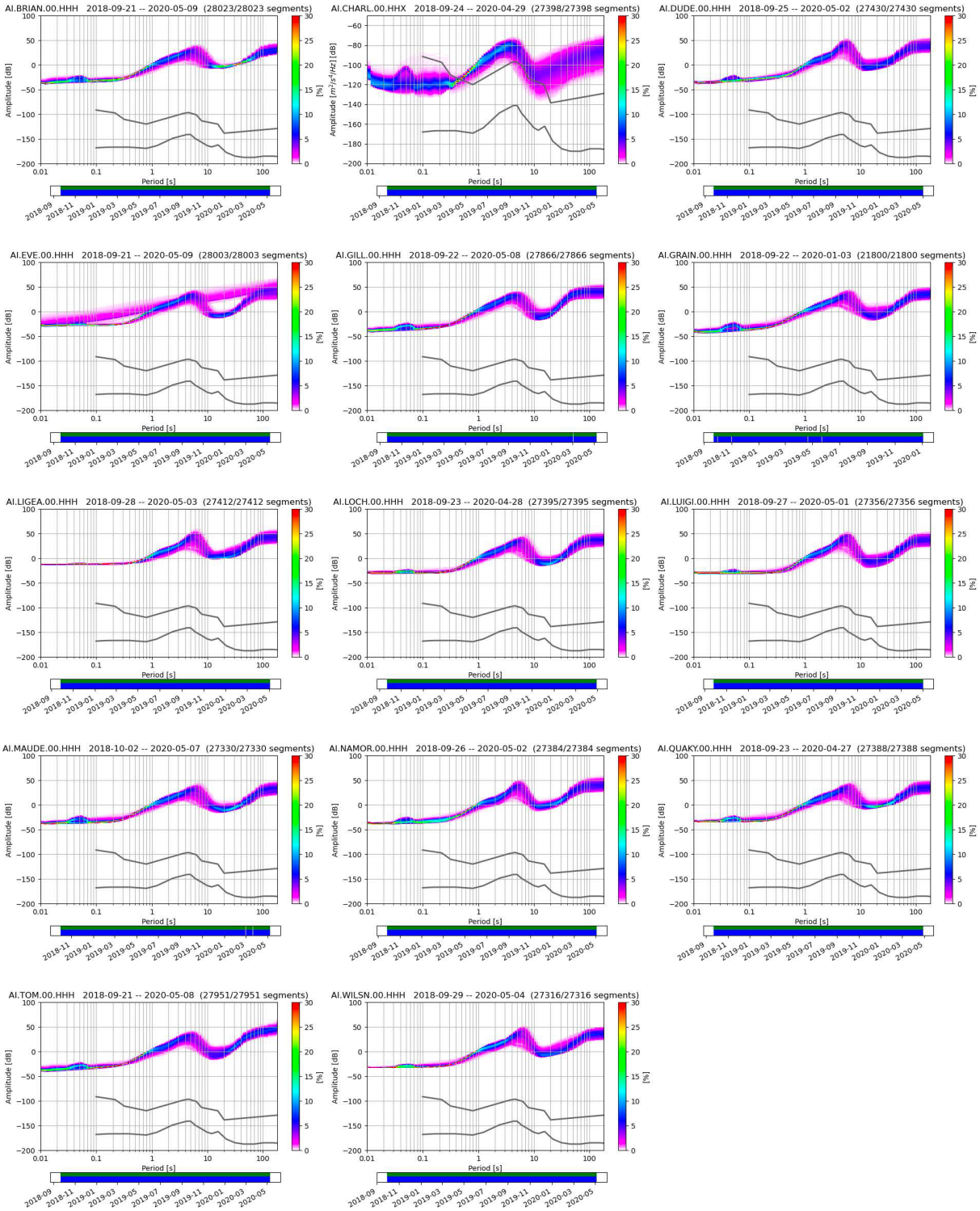

Figure A4. Probability power spectral density (PPSD) plots of the H (pressure) component of the 14 OBSs retrieved.

Appendix B. Orientation results

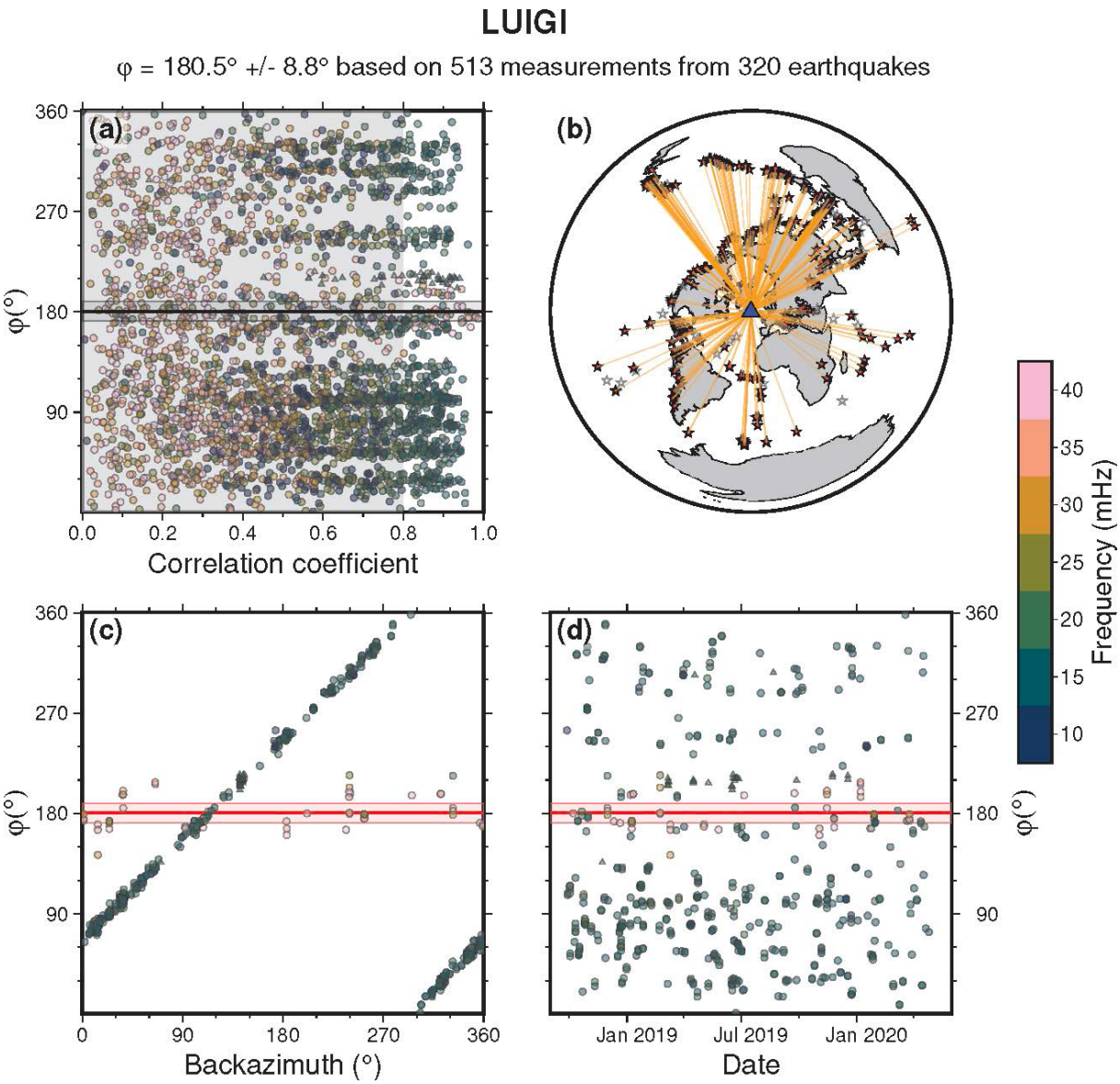

Figure B1. DLOPy orientation results for LUIGI. (a)-(d) same as for Fig. 5. In panel (c), the widely distributed lower-frequency results fall along a 1:1 line with backazimuth, indicating a constant oscillation that is unrelated to the earthquakes being used.

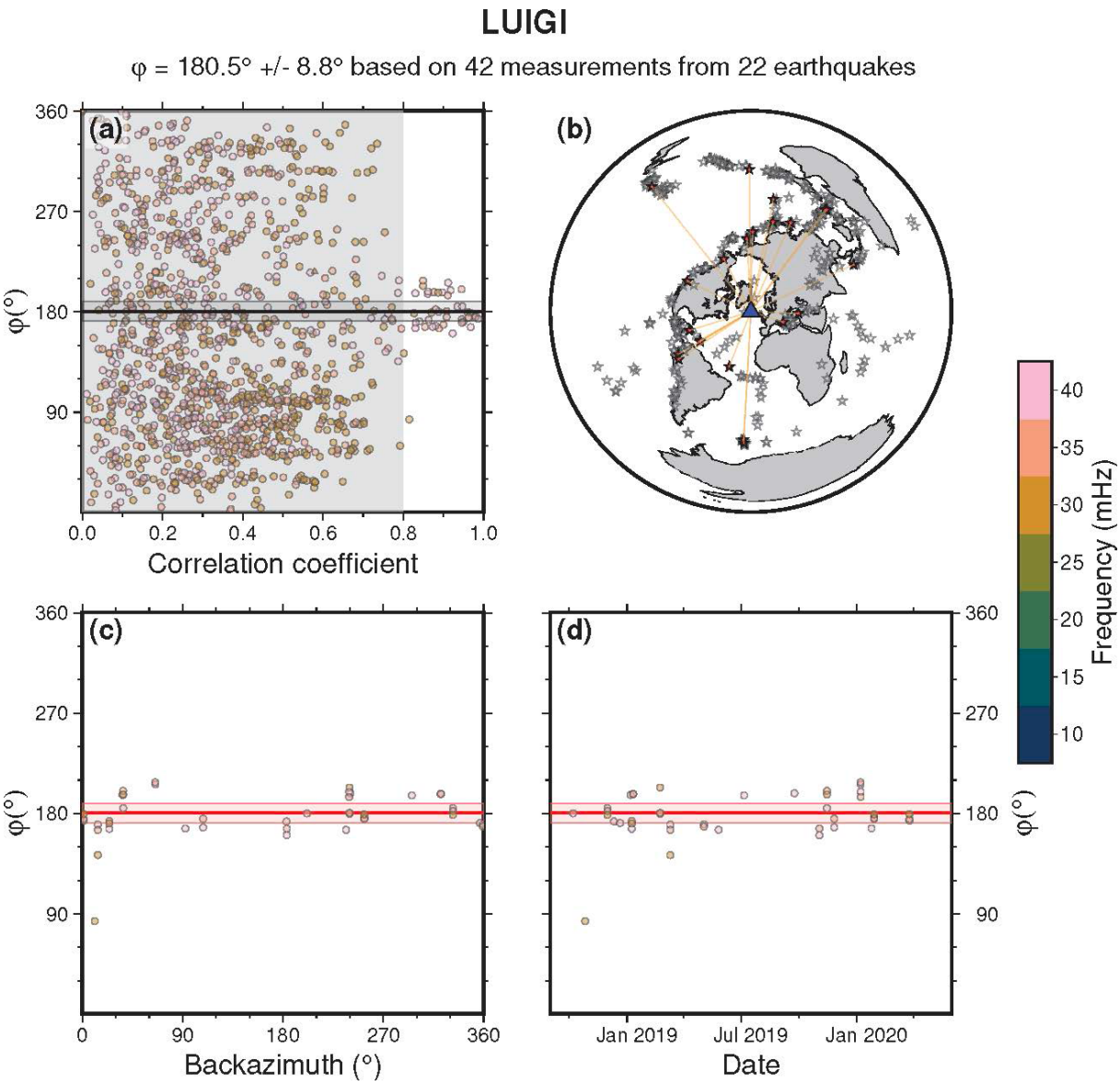

Figure B2. DLOPy orientation results for LUIGI, with the lower frequency bands (central frequency ≤25 mHz) removed, resulting in a stable orientation. (a)-(d) same as for Fig. 5.

***CORRESPONDING AUTHOR: Janneke Iza DE LAAT**,
Department of Applied Earth Sciences, ITC, University of Twente, Enschede, The Netherlands
e-mail: j.i.delaat@utwente.nl